

Hydrodynamic shock in Rivers: Physical and numerical modeling of flow structures in tsunami-like bores

Cite as: Phys. Fluids **35**, 106607 (2023); doi: [10.1063/5.0161096](https://doi.org/10.1063/5.0161096)

Submitted: 8 June 2023 · Accepted: 18 September 2023 ·

Published Online: 10 October 2023






View Online



Export Citation



CrossMark

Bruno Simon,^{1,2}  Pierre Lubin,^{1,2,3}  and Hubert Chanson^{1,a)} 

AFFILIATIONS

¹The University of Queensland, School of Civil Engineering, Brisbane QLD 4072, Australia

²University of Bordeaux, CNRS, Arts et Metiers Institute of Technology, Bordeaux INP, INRAE, I2M Bordeaux, F-33400 Talence, France

³Bordeaux INP, University of Bordeaux, CNRS, Arts et Metiers Institute of Technology, INRAE, I2M Bordeaux, F-33400 Talence, France

Note: This paper is part of the special topic, Shock Waves.

^{a)}Author to whom correspondence should be addressed: h.chanson@uq.edu.au. Tel.: (61 7) 3365 3619. Fax: (61 7) 3365 4599

ABSTRACT

The aim of this work is to provide convincing evidence on the turbulent processes induced by three-dimensional (3D) bores, based on physical and computational fluid dynamics studies of undular tidal bores, a phenomenon very similar to a tsunami-like bore propagating inland along a river. The numerical study is performed by solving the Navier–Stokes equations with a large eddy simulation method in order to access the turbulent flow evolution during the bore passage. Two- and three-dimensional simulations are performed with and without turbulence before bore generations to inspect the effect of coherent structures on the bore propagation. A complex three-dimensional flow takes place during the bore passage. Beneath the undulation crests, a strong shear is observed near the channel bed. Moreover, ejection of turbulent structures occurs during the propagation of undular bores depending on the initial flow conditions. These simulations provide the first detailed three-dimensional data of undular bores intricate flow structure. The results showed that the propagation of the bore front drastically changes the properties of the water column. It is also highlighted that for an upstream current exceeding a threshold value, near-bed eddies are generated and ejected in the water column independently of the free surface characteristics. Our simulations improve the understanding of positive surges which could be extended to tsunami-like bores studies.

Published under an exclusive license by AIP Publishing. <https://doi.org/10.1063/5.0161096>

I. INTRODUCTION

All the catastrophic events inherent to tsunamis reported in the literature have highlighted the extremely rapid propagation of tsunami waters along rivers and canals, causing very significant damage inland. A tsunami is an ocean wave triggered by volcanic eruptions, submarine landslide, onshore landslides in which large volumes of debris fall into the water, or large earthquakes occurring near or under the ocean. This infamous phenomenon takes the form of a shallow water wave of infinite wavelength, compared to the water depth of the water it is traveling through. Tsunamis propagate at high speeds and travel great, transoceanic distances with limited energy loss, thus striking coastlines from several continents for each recorded event. While tsunamis propagate in deep ocean water depths, they will slow down in speed and their amplitudes will dramatically increase as they reach the shorelines. [Madsen et al. \(2008\)](#) discussed the reproduction of tsunami-like bores in a variety of conditions. The amount of energy released in the catastrophic impact between the tsunamis and the landforms then cause

massive damage and casualties, as the waves break leading to the formation of walls of water running quickly over the land ([Yeh et al., 1996](#); [Hebenstreit, 1997](#)). Subsequently, large land areas can be inundated. After breaking, a tsunami wave propagating in shallow waters is preceded by a breaking front. In these shallow rivers and bays, the breaking bore propagation is associated with strong mixing and massive upstream sedimentary processes. [Arnason et al. \(2009\)](#) experimentally studied the interactions between a broken tsunami wave and structures of different cross sections and sought to further the understanding of interactions between the bore-like flow generated by a dam-break (DB) flow. If eventually a river mouth is located in the impacted area, the flooded areas can be much greater, due to the penetration of the tsunami in the river which can then travel inland on much larger distances ([Yeh et al., 2012](#); [Chanson and Lubin, 2013](#); [Tolkova et al., 2015](#); and [Tolkova, 2018](#)). Several examples have been documented on video (see Tsunami at Okawa River in Kesennuma city, video cited in reference), and many unsuccessful attempts have

been made to protect the coastal areas. [Liu et al. \(2013\)](#) documented several strategies locally implemented, as a “tsunami control forest” which was planted to protect the local community, or tsunami shelters to provide nearby and accessible shelter for people trying to escape from directly threatened areas. Moreover, a nearby river was armed with a tsunami gate, which was supposed to be closed in the event of an approaching tsunami. [Liu et al. \(2013\)](#) reported that all these strategies failed to protect against the 11 March 2011 Tohoku Tsunami event, supported by many pictures of the remains of the buildings, bridges and structures, which have been massively over-washed by the catastrophic event which exceeded the estimates in the designs. However, it remains impossible to perform any full scale measurements of the hydrodynamics of bores due to tsunamis.

[Chanson and Lubin \(2013\)](#) discussed the possible analogies between in-river tsunami bores and tidal bores, which is another intense and powerful natural phenomenon observed in rivers when the tidal flow turns to rising, leading to the generation of a positive surge propagating upstream the river to form the tidal bore. Even if a tsunami and a tidal wave are obviously two different and unrelated phenomena, both present very similar features when propagating in shallow waters, and even more upstream rivers. Both tsunami and tidal bores are defined as a hydrodynamic shock wave progressing upstream in estuaries and rivers. A tidal bore is a specific type of positive surge propagating upstream estuaries and rivers ([Fig. 1](#)), appearing at the leading front of the rising tide as it propagates upstream estuaries. Its propagation induces large turbulences and sediment resuspension ([Khezri, 2014](#); [Simon, 2014](#); [Furgerot, 2014](#); [Leng, 2018](#); and [Shi, 2022](#)). Famous tidal bores include the Silver Dragon bore in the

Qiantang River (China), the Pororoca in the Amazon River (Brazil) and the Bono in the Kampar River (Indonesia) ([Chanson, 2011a](#)). In the Qiantang River, bores could reach a height of 6 m ([Bartsch-Winkler and Lynch, 1988](#)) while in India, bores could propagate at a celerity of 12 m s^{-1} (given a 10.7 m s^{-1} analytic estimation) ([Chugh, 1961](#)). Recently, tidal bores have gained in popularity by the release of surf videos and the increase in news coverages. Several reasons make tidal bores attracting: their large size, the roaring sound they make, the scenic spectacle Nature offers, the folklore associated or their shape variations. Bores can take various form but two shapes are most recognizable: the undular bore, when the wave consists of a series of undular whelps and the breaking bore, when a breaking roller rushes loudly upriver without undular waves following the front. As [Fig. 1](#) illustrates, the shape can be more complex when breaking roller forms on the crest of the undulations making the bore a mix of undular and breaking. [Figure 1](#) also shows that many surfers come to surf a wave that propagates for far longer than classical wave. There are even more surfers when bores form at their biggest sizes when river conditions combine spring tides and low-water discharge usually during summer ([Chanson, 2011a](#)). This is also the occasion for tourists to watch a unique show that local populations consider as a cultural heritage organizing special events and celebrations during “bore season.” [Figure 2](#) presents sketches and photographs of breaking and undular bores.

The phenomenon also has an impact on other human activities and on the life of the estuarine system in terms of flow management ([Jiang et al., 2014](#)), navigation ([Moore, 1893](#)), and wildlife ([Rulifson and Tull, 1999](#)). Therefore, the studies on tidal bores have increased. Simple visual observations show that tidal bores participate in the



FIG. 1. Sequence of a tidal bore propagating in the Dordogne River at Vayres, 2011-04-21 (Photos: B. Simon). The bore is undular with some breaking happening on the wave crest. Most surfers are riding the bore front wave. The sequence read from left to right with photos every 2 s.

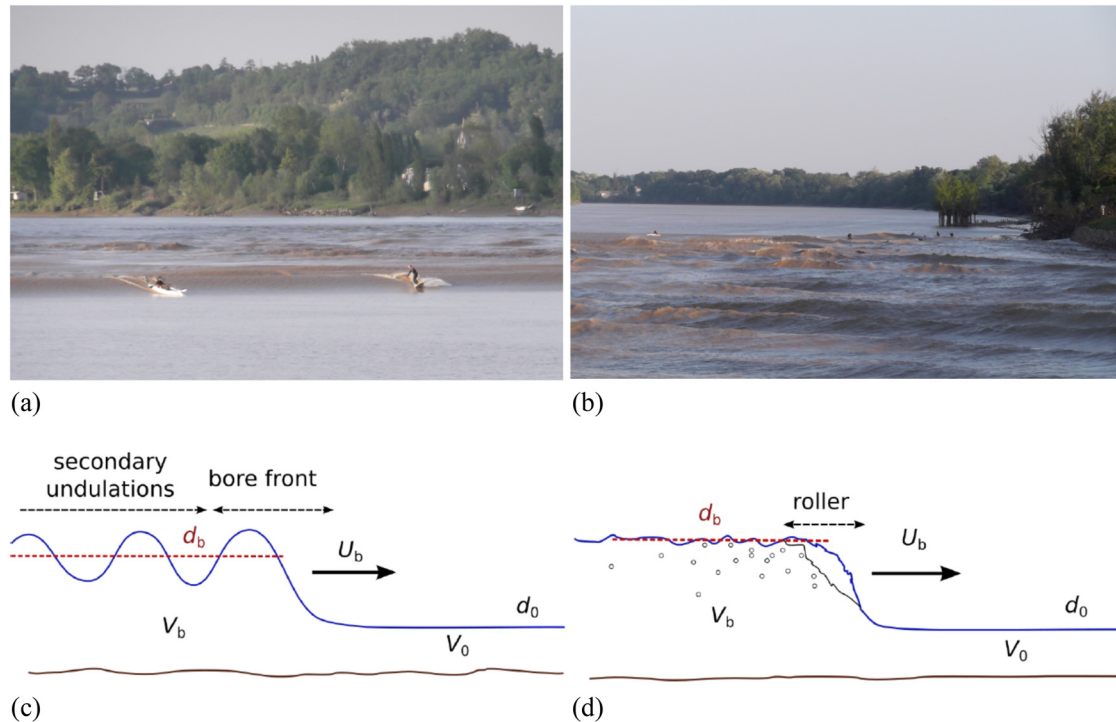


FIG. 2. Photography of an undular tidal bore and sketches of the two main shapes taken by positive surges: undular bore (1c) and breaking bore (1d). d_0 , d_b , V_0 , V_b are the water depths and the main current velocities respectively before (subscript 0) and after the bore passage (subscript b), U_b is the bore celerity. (Photos: B. Simon). (a) tidal bore arrival, (b) back side of a tidal bore, (c) undular bore, (d) breaking bore.

mixing and resuspension of sediments and large particles. This is induced by the rapid and lasting flow reversal observed following the bore passage and causing an intensification of the turbulence (Chanson *et al.*, 2011; Simpson *et al.*, 2004; and Furgerot *et al.*, 2013; 2016). The sudden change in flow conditions due to the bore induces an increase in sediment concentration (Chanson *et al.*, 2011; Mouaze *et al.*, 2010; and Keevil *et al.*, 2015), as well as the resuspension of fish eggs (Rulifson and Tull, 1999; Chanson and Tan, 2010) and the dispersion of microfossils (Laut *et al.*, 2010). The effects of the bore are known, but the structure of the flow beneath the free-surface and the subsequent processes are yet to be completely detailed and analyzed. Numerical models give the opportunity to study tidal bore in controlled domains with selected parameters, and without damaging or losing equipment (Simpson *et al.*, 2004; Mouaze *et al.*, 2010; and Reungoat *et al.*, 2014) or encountering dangerous animals (e.g., crocodiles, sharks, snakes), as it previously happened in the field (Wolanski *et al.*, 2004). A complex three dimensional flow takes place during the bore passage (Fig. 2). Beneath the undulation crests, a strong shear is observed near the channel bed. Moreover, ejection of turbulent structures occurs during the propagation of undular bores depending on the initial flow conditions. However, despite the strong impact of the mixing on the wildlife and the river sediment transport, the turbulent mechanisms involved still need to be detailed. This is due to the limited numbers of observations and the difficulty to obtain detailed measurements.

Beneath the free surface, a complete flow reversal usually occurs as the bore passes (Chanson *et al.*, 2011; Mouaze *et al.*, 2010; and Simpson *et al.*, 2004). Nevertheless, it was also observed that the

current dynamics can be different from just a reversal with the front (Darcy and Bazin, 1865; Reungoat *et al.*, 2014; 2017). For example, downstream a meander, a bore can split into two fronts, with a first front producing a flow deceleration with no change of direction and the second front inducing a flow reversal (Kjerfve and Ferreira, 1993). Another example is an island dividing the river in a main channel and a smaller branch: the bore front might split between the main river course and the smaller channel, with the faster bore in the main channel entering the arm at its upstream end and forming a counter-bore (Bonneton *et al.*, 2011b; Keevil *et al.*, 2015). Most studies, including the present study, try to determine the kernel of the phenomenon with a simple geometry, simple flow considerations and focusing on the moment just before and after the bore passage. The simplest geometry is a rectangular channel with constant dimensions. A few recent experimental works can be highlighted where trapezoidal channel have been used to study the transverse mixing induced by unsteady secondary motion (Kiri *et al.*, 2020a; 2020b; Fernando *et al.*, 2020) and will be discussed in Sec. VI of this paper to highlight the perspectives of future works.

Experimental studies in a straight rectangular channel have confirmed that the bore passage may induce in some cases a flow reversal beneath the bore as well as an increase in flow turbulence (Koch and Chanson, 2008; Leng, 2018; and Shi, 2022). However, such studies were mostly conducted with intrusive probes providing pointwise measurements. During the recent decades, studies have been devoted to the characterization and quantification of the turbulent and sediment mixing processes occurring when tidal bores propagate upstream rivers. Recently, Kobayachi and Uchida (2022) investigated

experimentally and numerically the characteristics of breaking bore in meandering channels, focusing on Froude number consideration. The laboratory experiments were conducted with different Froude number conditions, comparing the meandering channel results with the straight channel results. They also qualitatively explained the factors which could limit the applicability of 2D calculations, comparing 3D calculations using a RANS model.

Numerical simulations can, thus, complement laboratory and field studies, and provide details of the flow evolution in the whole domain of propagation, even considering such a simple configuration than a rectangular channel. Several studies were performed by solving the Saint-Venant equations (Madsen *et al.*, 2005), Boussinesq equations (Abbott and Rodenhuis, 1972; Castro-Orgaz and Chanson, 2022), Serre-Green-Naghdi equations (Castro-Orgaz and Chanson, 2020; Roy-Biswas *et al.*, 2021), the 3D Reynolds-averaging Navier–Stokes equations (Ai *et al.*, 2021) or Korteweg–de Vries equations (Peregrine, 1966; Bjørnstad *et al.*, 2021). Solving these equations gives good approximations for the free-surface, but it does not yet investigate the intricate flow hydrodynamics. Flow reversal and increase in turbulent levels are not taken into account by the previously cited equation systems. However, the Navier–Stokes (NS) equations can model the flow in bores with great details, as shown in previous two-dimensional numerical simulations of breaking bores (Lubin *et al.*, 2010a; 2010b; Furuyama and Chanson, 2008). These studies of breaking bores showed the apparition and ejection of large recirculation structures above the channel bed following the wake of the bore front, but remained simplified two-dimensional studies. Moreover, Ai *et al.* (2021), using a 3D non-hydrostatic model, simulated undular bores in open channels. The model was validated with four typical benchmark problems: undular bore development, an undular bore generated by a sudden discharge, dam-break flow over a triangular bottom sill, and dam-break flow through an L-shaped channel. They showed the capacity of the model to simulate the hydrodynamic features of the flow. The effect of tidal rise on tsunami waves was addressed by Kalmbacher and Hill (2015), using depth-averaged equations, while the effect of channel shape was addressed for a broad class of tsunami-like-long-waves by Winckler and Liu (2015), solving Boussinesq-type equations. Kang *et al.* (2011) simulated the complex structure of the flow in terms of primary and secondary vortices in

curved areas of the channels. They discussed the comparison of direct numerical simulation (DNS), large-eddy simulation (LES), or unsteady Reynolds-averaged Navier–Stokes (URANS) modeling, in the case of a 50 m long natural meandering stream using a resolution sufficiently fine to capture vortex shedding from centimetre-scale roughness elements on the bed. Later, Putra *et al.* (2019) studied the impact of tidal bores on the transport of non-cohesive sediment particles on the basis of the earlier works of Berchet *et al.* (2018), while Roy-Biswas and Sen (2022) presented a systematic assessment of 2D RANS models compared with 2D LES results on positive surge modeling, showing the great capabilities of such models to successfully describe the hydrodynamics beneath the free-surface.

Our present numerical study was based on data from selected laboratory experiments (Chanson, 2010b; 2012). However, it must be noticed that several types of positive surges exist: tidal bores, dam break wave (Marche *et al.*, 1995), stationary hydraulic jump (HJ) (Andersen, 1978) and surges generated by rejection of a flow against an obstacle and propagating upstream (Chanson, 2010b; Koch and Chanson, 2009; and Simon and Chanson, 2013) (Fig. 3). In this paper, we chose the latter since the bore is propagating against an adverse flow, similarly to most cases in rivers, to detail the 3D turbulent processes under undular bores. Experimental pictures are shown on Figs. 4 and 5 to show the closure of the downstream end gate and the bore propagation, respectively.

Most tidal bore field studies show an opposite flow (OF) sketched in Fig. 3. Surprisingly, when the hydrodynamic effects of the tsunami-like bores (TBs) passage are studied in hydraulic flume either experimentally (Treske, 1994) or numerically with computational fluid dynamics (CFD) (Furuyama and Chanson, 2008; Madsen *et al.*, 2005; and Lubin *et al.*, 2010a; 2010b), the studies are based on either dam break (DB) wave, where the wave propagates against still water (Hornung *et al.*, 1995; Marche *et al.*, 1995; and Soares Frazao and Zech, 2002), or a bore generated by placing an obstacle downstream the flume which in turn produces an upstream positive surge, whether the channel is fully closed (FC) or partially closed (PC) (Benet and Cunge, 1971; Khezri and Chanson, 2012; and Koch and Chanson, 2008). Yet, for a similar Froude number, the shape, determined by the wave amplitude or length, of the free surface could be different depending upon the test case (as in Fig. 3 in Khezri and Chanson,

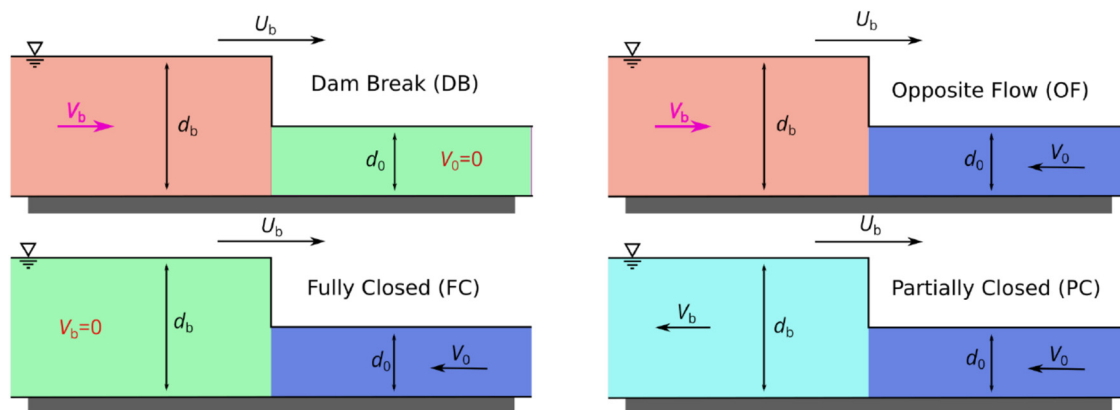


FIG. 3. Definition sketch of TBs propagating from left to right for an observer standing still. $d_b > d_0$, $U_b > 0$, $V_0 \leq 0$, whereas V_b is positive or negative.

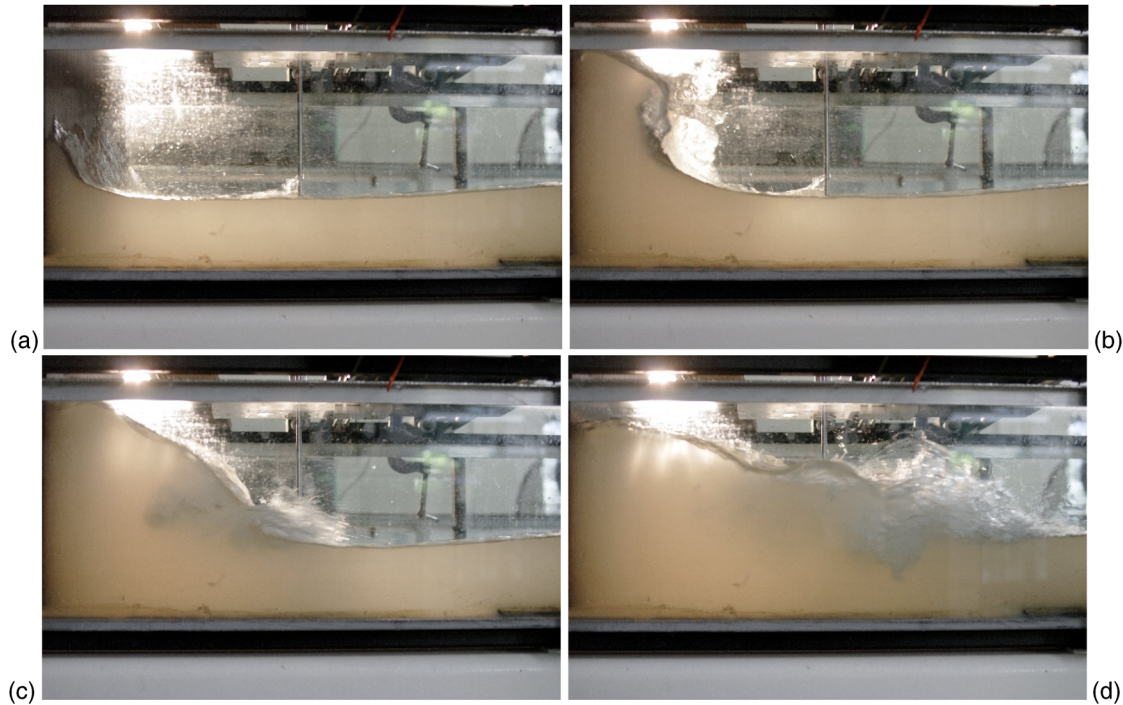


FIG. 4. Bore generation by rapid tainter gate closure, with upstream bore propagation from left to right— $Q = 0.0537 \text{ m}^3/\text{s}$, $d_0 = 0.114 \text{ m}$, $S_0 = 0.00773$, $h_g = 0.009 \text{ m}$, photographed between $x = 10.2$ to 11.15 m , with 192 ms between two successive frames (Simon and Chanson, 2013). (a) Flow impacting the closing gate. (b) Surge initiation with a first breaking event. (c) Surge propagating against the river flow with a first splash-up. (d) Air entrained as the bore front is progressing towards the upstream end of the channel.

2012). Previous simulations (Simon, 2014) showed that, for nearly identical Froude numbers, an inversion of the flow near the bed could occur for a PC case or not DB case. One parameter that could influence such differences might be the flow field upstream and downstream the bore.

Herein, a numerical study of undular bores is realized with simulations in two and three dimensions, and the data are compared to experimental results. The numerical study is performed by solving the Navier–Stokes equations with a large eddy simulation method in order to access the turbulent flow evolution during the bore passage. Two- and three-dimensional simulations are performed with and without turbulence before bore generations to inspect the effect of coherent structures on the bore propagation. These simulations provide the first detailed three dimensional data of flow turbulence for undular bores. In this paper, we aim to propose a numerical study to illustrate the hydrodynamics considering different types of bore generation, and provide a thorough discussion on the turbulent processes observed under undular bores, compared to the most recent works. First, we will introduce the equations and the numerical methods, including the method used to inject the turbulent experimental conditions in the 3D numerical simulations. Then, before showing 2D numerical results, the analytical definition of the Froude number is discussed. Based on the Froude number, 2D dam-break bore test-case is validated, and a 2D positive surge is compared to experimental data. Follows a discussion on different techniques used to generate bores (dam-break, reflection wave due to an opposing flow, or a partially closed gate, or a fully closed gate, hydraulic jump). Then, the 3D numerical results are

presented, leading to a section dedicated to a discussion and some perspectives will be provided as a conclusion.

II. NUMERICAL MODELING

A. Equations and numerical methods

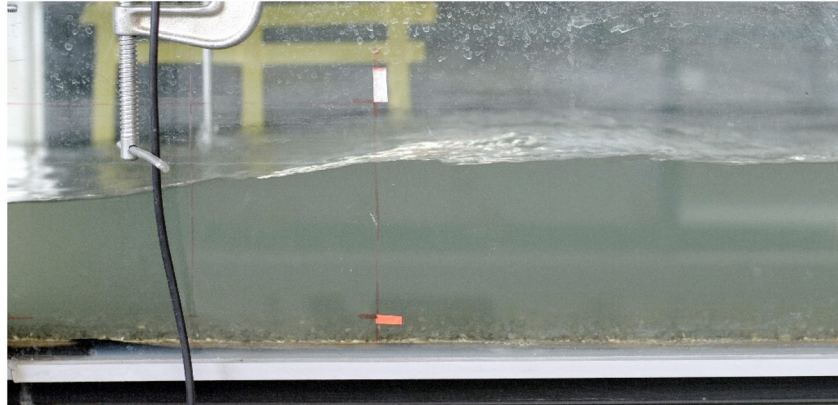
To simulate the detailed hydrodynamics and turbulence of positive surges, the Navier–Stokes (NS) equations, in their multiphase forms (Kataoka, 1986), were solved using the CFD code Thetis (home-made numerical tool from the University of Bordeaux, as of 2015: Notus, for the open-source version). Since the Reynolds number for the present simulations is greater than 9×10^4 , a Large Eddy Simulation (LES) filter is used with the NS equations (Sagaut, 2006). The air/water interface was tracked by a Volume Of Fluid (VOF) method using a Piecewise Linear Interface Calculation model (Youngs, 1982). The system of equations yields

$$\nabla \cdot \mathbf{u} = 0, \quad (1)$$

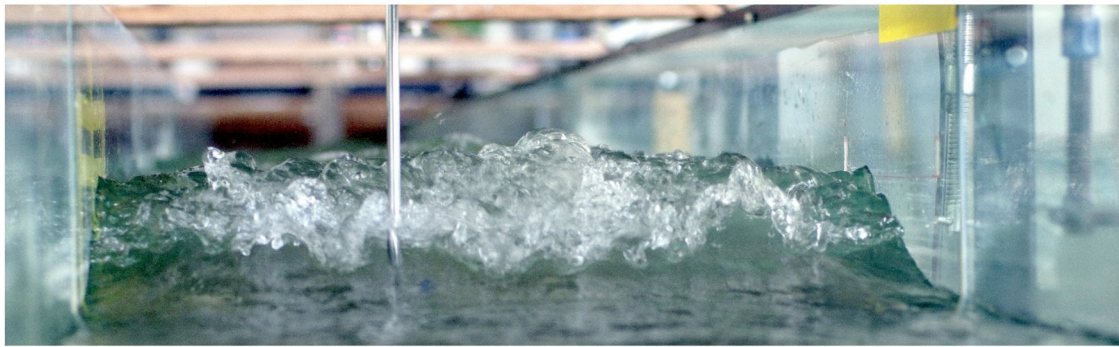
$$\rho \left(\frac{\partial \mathbf{u}}{\partial t} + (\mathbf{u} \cdot \nabla) \mathbf{u} \right) = \rho \mathbf{g} - \nabla p - B_u - \frac{\mu}{K} \mathbf{u} + \nabla \cdot \left[(\mu + \mu_t)(\nabla \mathbf{u} + \nabla^T \mathbf{u}) \right], \quad (2)$$

$$\frac{\partial C}{\partial t} + \mathbf{u} \cdot \nabla C = 0, \quad (3)$$

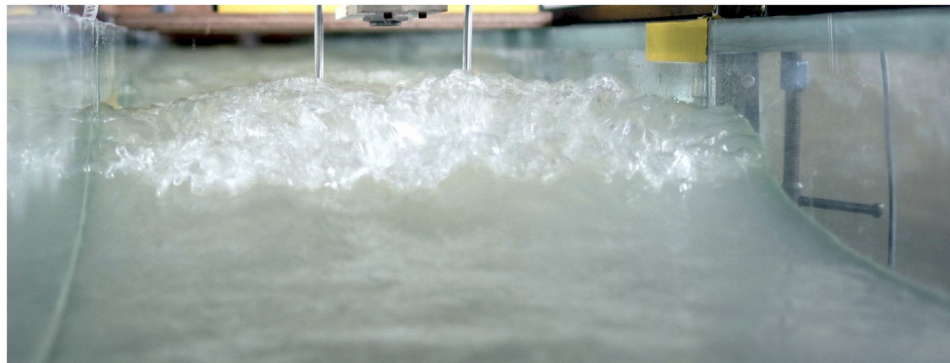
with \mathbf{u} being the filtered velocity vector, p the pressure, μ the fluid viscosity, ρ the fluid density, μ_t the turbulent viscosity, B_u a matrix forcing the velocity components on the boundary, and K a permeability



(a)



(b)



(c)

FIG. 5. Photographs of upstream bore propagation in the rectangular channel (Simon and Chanson, 2013): (a) Undular bore ($Fr = 1.3$) propagating from left to right— $Q = 0.0364 \text{ m}^3/\text{s}$, $d_o = 0.084 \text{ m}$, $h_g = 0.043 \text{ m}$. (b) Breaking bore ($Fr = 1.6$)— $Q = 0.0364 \text{ m}^3/\text{s}$, $d_o = 0.084 \text{ m}$, $h = 0 \text{ m}$. (c) Breaking bore ($Fr = 1.7$)— $Q = 0.0536 \text{ m}^3/\text{s}$, $d_o = 0.114 \text{ m}$, $h = 0$. Note two ADV units mounted side-by-side.

coefficient. The gravitational vector \mathbf{g} is set to $\mathbf{g} = 9.81 \text{ m s}^{-2}$. The turbulent viscosity is calculated thanks to the Mixed Scale model (Sagaut, 2006), which is derived from a weighted geometric average of the classical Smagorinsky subgrid scale model (Smagorinsky, 1963) and the turbulent kinetic energy subgrid scale model (Bardina *et al.*, 1980).

The VOF-PLIC method has the advantage of building a sharp interface between the air and the water. The phase function C is used to locate the different fluids. The magnitude of physical characteristics of the fluids depends on the local phase. The physical characteristics are defined according to C as

$$\begin{aligned}\rho &= C\rho_w + (1 - C)\rho_a, \\ \mu &= C\mu_w + (1 - C)\mu_a,\end{aligned}\quad (4)$$

where $\rho_a = 1.1768$ and $\rho_w = 1000 \text{ kg m}^{-3}$ are the densities and $\mu_a = 1.85 \times 10^{-5}$ and $\mu_w = 1 \times 10^{-3} \text{ kg m}^{-1} \text{ s}^{-1}$ being the viscosities of air and water, respectively. Since the phase function is not defined at each point where the viscosities and densities are needed for the Navier–Stokes discretization, the physical characteristics are interpolated on the staggered grid corresponding to the marker and cell method. The density on the velocity nodes is calculated with a linear interpolation, whereas harmonic interpolation is used for the viscosity. Time discretization of the momentum equation is implicit and a Euler scheme is used. The velocity/pressure coupling under the incompressible flow constraint is solved with the time splitting pressure correction method (Goda, 1979). The equations are discretized on a staggered grid by means of the finite volume method. The space derivatives of the inertial term are discretized by a hybrid upwind-centered scheme, whereas the viscous term is approximated by a second-order centered scheme (Patankar, 1980). The MPI library is used to parallelize the code, the mesh being partitioned into equal size subdomains to ensure load balancing. The HYPRE parallel solver and preconditioner library is used to solve the linear systems (Falgout *et al.*, 2006). For faster simulations, the domain was partitioned into 32 subdomains, with one processor per subdomain. The numerical code was previously extensively verified and validated through numerous test-cases, including mesh refinement analysis for coastal applications (Lubin and Glockner, 2015) and sediment transport by tidal bores (Berchet *et al.*, 2018) using numerical data from Simon (2014) as inlet boundary conditions. Moreover, Putra *et al.* (2019) used the open-source software OpenFOAM and successfully compared the numerical results from Thetis, OpenFOAM, using similar numerical settings that those chosen in this study, against several sets of experimental and analytical data, thus validating our numerical approach.

B. Turbulent inflow conditions for the 3D numerical simulations

To numerically reproduce a turbulent inflow condition, as generated in physical experiments, the numerical code required some turbulence injection in the numerical domain. We chose to use the Synthetic Eddy Method (SEM) (Jarrin *et al.*, 2006; Jarrin, 2008; Chanson *et al.*, 2012; Simon, 2014; and Leng *et al.*, 2018) since it is a relatively simple and efficient method (Dhamankar *et al.*, 2018). It explicitly generates large-scale coherent structures and convects them with the mean flow through the inlet plan. This method considers turbulence as a superposition of coherent structures. These eddies are generated over the inlet plane of the calculation domain and defined by a shape function that encompasses the spatial and temporal characteristics of the targeted structures. To compute a coherent stochastic signal, the method only requires the mean velocity and the Reynolds stresses, which are obtained from the experimental data, and the typical size and number of eddies, which can be roughly estimated as detailed by Jarrin *et al.*, 2006. Although the SEM involves the summation of a large number of eddies for each grid point on the inflow, the central processing unit (CPU) time required to reconstruct a fluctuating inflow condition corresponding to the experimental one for each iteration is negligible. The SEM reconstructs the velocity signals by adding the velocity fluctuation \mathbf{u}' to the mean velocity $\bar{\mathbf{u}}$. The velocity

is computed, as indicated by Jarrin *et al.* (2006), and the SEM method is reported to perform well on any geometry and for any kind of flow.

The SEM generates eddies in an extra sub-domain, also box of eddies, as coined by Jarrin *et al.*, 2006, of the main simulation domain. The velocity signal is extracted from this sub-domain and added to the main simulation. At each time step of the main simulation, the SEM transports eddies within its sub-domain with the modeled velocity. When eddies are convected outside of the sub-domain new eddies are added to maintain their number. The signal generated is thus a stationary ergodic random process. The SEM reproduces the same mean velocity and Reynolds stresses as those given in input. Yet, the turbulence recovers a coherent value after a distance of about 15 times half the SEM's inlet (Jarrin, 2008) during which the turbulence decreases (Simon, 2014). In our 3D numerical simulations, the flow velocity and Reynolds stresses were reconstructed from polynomial approximations of measured vertical profiles realized independently (Chanson, 2010b; 2011b). The measurements were made at $x = 7.2 \text{ m}$ from the inception zone of the bore, but the recreated turbulence was injected in the numerical domain at $x = 10 \text{ m}$ (see Sec. IV).

C. Froude number definition

Focusing only on the instant before and after the bore passage, the bores are upstream positive surges, i.e., a sudden increase in the water level and a sudden change of the current. Figure 3 presents sketches of the various flow conditions associated with upstream positive surges propagation where a bore travels at velocity $U_b > 0$ upstream a body of water with a depth d_0 and a velocity $V_0 \leq 0$. The mean water level after the bore, or bore conjugated depth, being d_b , and the bore flow velocity being V_b , either positive or negative. Figure 4 displays an example of the bore generation by the closure of a Tainter gate, fully closed and vertical. Figure 5 presents pictures of an example of experiments conducted in the physical channel of the University of Queensland. The bore is propagating upstream against the initially steady flow and physical observations were conducted about mid-channel (Simon and Chanson, 2013).

A summary of the basic flow dynamic in a positive surge are listed in Table I with common applications. Although it has also been used as an analogy for tsunami bore (Chanson, 2009a), the case of the static hydraulic jump (HJ) is excluded from this discussion since the bore is not traveling ($U_b = 0$) as a tsunami-induced bore. Tsunami bores and other positive surges can be solely breaking, or solely undular or can have some weak breaking on the wave crests. In any case, the propagation of a positive surge can be simplified assuming a

TABLE I. Simplification of the flow dynamics for positive surges (see Fig. 3).

V_0	V_b	U_b	Applications	Abbreviations
0	>0	>0	Dam break wave	DB
<0	>0	>0	Tsunami bores, Tidal bores	OF/TB
<0	0	>0	Reflection wave on a fully closed gate	FC
<0	<0	>0	Reflection wave on a partially closed gate	PC
<0	<0	0	Stationary hydraulic jump	HJ

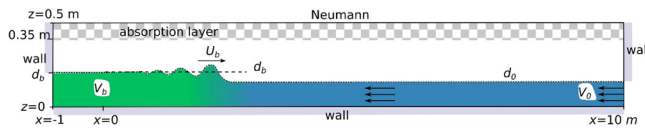


FIG. 6. Sketch of the 2D numerical domain, showing the boundary conditions used for the simulations. The right side of the numerical domain is upstream (river flowing downstream) and the left side is downstream (where the tidal flow rises upriver). The flow conditions consist in two rectangles of water initialized with velocities V_0 and V_b before and after $x = 0$ m. The V_0 velocity is either positive (DB—dam break; OF—opposite flow; PC—partially closed gate) or negative, depending on the cases modeled (see Table II and Fig. 3), while V_b is always negative (modeling the river flowing from downstream to upstream). The resulting hydrodynamic shock is visible as a positive surge is generated with a positive velocity. U_b is always positive, indicating the bore front traveling from downstream to upstream.

horizontal bottom, hydrostatic pressure and no bed friction. Under the previous hypotheses and since the flow upstream (subscript 0) and downstream (subscript b) the front must satisfy the continuity and momentum principles, we can obtain a series of relationships between the flow properties after integration (Barre de Saint Venant, 1871; Rayleigh, 1908), for a system of reference moving with the bore, as follows:

$$(V_0 - U_b)d_0 = (V_b - U_b)d_b, \quad (5)$$

$$\rho g(d_0^2 - d_b^2) = 2\rho d_0(V_0 - U_b)(V_b - V_0), \quad (6)$$

where ρ is the fluid density and g is the gravitational acceleration. The combination of the continuity and momentum equations gives (Henderson, 1966; Chanson, 2012)

$$\frac{d_b}{d_0} = \frac{1}{2}(\sqrt{1 + 8Fr^2} - 1), \quad (7)$$

where Fr is the surge Froude number defined in a horizontal rectangular channel as

$$Fr = \frac{|V_0 - U_b|}{\sqrt{gd_0}}. \quad (8)$$

We will evaluate the impact of both V_0 and V_b as initial conditions on positive surges hydrodynamics, through a 2D numerical exercise. The numerical simulations are performed after selecting an initial water depth d_0 and a Froude number Fr . Choosing an initial Froude number sets the ratio d_b/d_0 [Eq. (7)] and choosing an initial value for the water depth d_0 then sets the initial value for d_b , which, in turns, set the value of $(V_0 - V_b)$, since

$$g(d_0^2 - d_b^2) = 2d_0Fr\sqrt{gd_0}(V_b - V_0). \quad (9)$$

All that is left to choose to perform simulations is one of the three initial values for V_0 , V_b or U_b in order to get the remaining two which will fulfill Eqs. (5) and (6). We set the initial water depth $d_0 = 0.1$ m, and for different Froude numbers and various values for V_0 , which set the initial type of flow according to Table I, we present the subsequent flow hydrodynamics in order to discuss and clarify the impact of the choices for V_0 and V_b when tsunami bores are studied, especially since V_0 and V_b are mostly observed to be in opposite directions in natural processes. We will take the advantages of the present numerical study, to make a comparison of various method to mimic a tidal bore, and discuss the subsequent flow features.

D. 2D Dam-break surge wave (DB)—Analytical validation

Before further discussing the numerical results of bore generation conditions, we illustrate the capacity of the numerical tool to handle hydrodynamic shocks as later studied in this article. We chose to validate our numerical results against analytical data, i.e., the dam-break (DB) problem over a wet bed. The DB wave is a classic case of bore generation and propagation, which allows to generate a bore and also provides an analytical solution (Lubin, 2004; Furuyama and Chanson, 2008; Simon, 2014; Putra et al., 2019; and Barranco and Liu, 2021; 2023), independently of any experimental dynamic inlet boundary conditions of any kind (so the SEM method is not required here). Indeed, the generation process consists of a high reservoir of water into a shallower water (Fig. 6). Analytical formulas give the bore celerity U_b and conjugate depth d_b knowing only the water depth at rest, d_0 , the water depth in the dam reservoir, d_1 , under the hypothesis of Eqs. (5) and (6) and in an infinitely long dam reservoir (Stoker, 1957; Montes, 1998). The computational fluid dynamics (CFD) code is compared with analytical values before discussing the hydrodynamics generated while the subsequent bore propagates. Figure 7 presents the initial flow conditions and the hydrodynamics of the propagating bore in the whole domain and the bore propagation.

The dam break is initialized with two zones of quiescent water with a hydrostatic pressure distribution separated by an infinitely thin wall. The higher dam reservoir has a water depth $d_1 = 0.158$ m while the small reservoir is $d_0 = 0.1$ m (Fig. 7). The 2D numerical domain is 20 m long and 0.5 m high. At the instant $t = 0$ s, the dam wall located at $x = 0$ m disappears instantaneously.

The domain boundaries are set with no slip boundary conditions. In the vertical direction, the mesh grid consists of 500 irregular meshes,

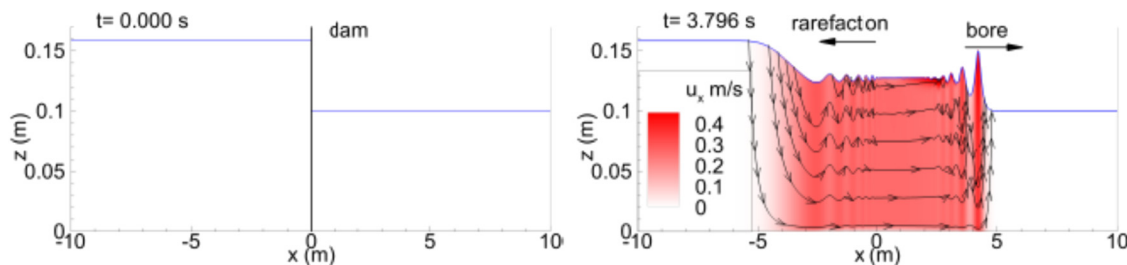


FIG. 7. Initial condition of the dam break case (DB) and wave propagation in the domain. Mapping of the longitudinal velocity with streamlines.

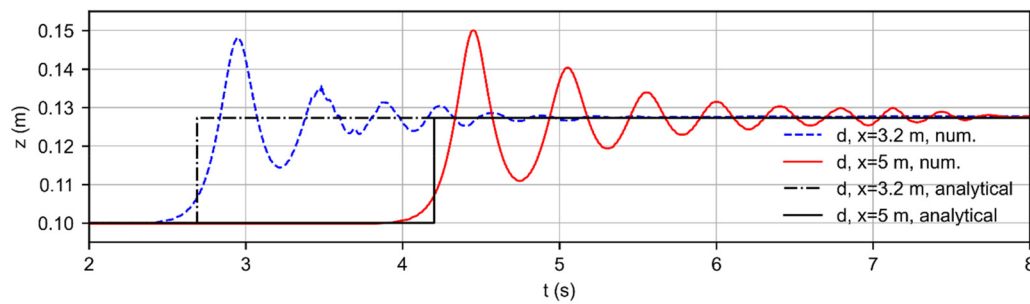


FIG. 8. Time evolution of the numerical free surface time evolution (num.) compared with theoretical values (analytical) at two different locations.

with Δz_{\min} starting at 5×10^{-5} m at the bottom and increasing exponentially to the top. In the longitudinal direction, between $x = 0$ and 10 m, the domain is discretized with 4100 regular cells. Whereas between $x = 0$ and -10 m, 500 non-constant meshes are used with exponential variation, starting with $\Delta x_{\min} = 2.4 \times 10^{-3}$ m at $x = 0$. The Courant–Friedrichs–Lewy (CFL) condition is inferior to 2/3 to ensure the scheme stability. It took approximately 20 h to perform the parallel simulation with 36 processors. With $d_1 = 0.158$ m and $d_0 = 0.1$ m, the theory [Eqs. (5)–(9)] predicts a bore with $U_b = 1.191$ m s^{-1} and $d_b = 0.1273$ m. Figure 8 presents the time series of the free surface elevations, showing the numerical results compared to the theoretical bore front position and elevation, and the following wave trains. The simulated bore is undular, with $Fr = 1.20$. As the bore propagates, secondary undulations form and oscillate around d_b with the wave train tail converging toward d_b . The free surface perturbation, produced by the collapse of the dam, remains slightly visible at $t = 3.5$ – 3.7 s in the time series measured at $x = 3.2$ m, but later disappears as the bore propagates. The numerical results also show that the bore accelerates progressively to reach a celerity value that is almost constant after the front passes $x = 2.5$ m. The numerical results yield $U_b = 1.190$ m s^{-1} and $d_b = 0.1275$ m at $x = 3.2$ m. We can then compare the celerity of an idealized bore to the numerical results of an undular bore to demonstrate the results are reasonable, however it has to be mentioned that the undular bore is transient such that its form (i.e., number of secondary undulations or whelps) and the wave celerity (i.e., U_b here) evolve with propagation distance (Brühl *et al.*, 2022), whereas an idealized bore has constant values as shown here.

Figure 9(a) presents the longitudinal velocity component time evolutions during the bore passage at several depths. Figure 9(b) presents a vertical profile of the longitudinal velocity underneath the first crest of the bore. The flow is observed to accelerate during the bore passage. Underneath the bore, the longitudinal velocity component oscillates around a mean value $V_b = 0.255$ m s^{-1} for $z > 0.02$ m, which is similar to the analytical data V_b . For $z < 0.02$ m, the longitudinal velocity component oscillates around a mean value depending on the depth. Marche *et al.* (1995) observed similar velocity profiles beneath the wave crest of a breaking DB wave.

Figure 10 shows the comparison between the simulated pressure evolution to the hydrostatic pressure calculated from the simulated free surface evolution at $x = 5$ m. Compared to the hydrostatic pressure, the simulated pressure field is lower beneath the crest and larger beneath the troughs (Fig. 10). Such a behavior is predicted by the irrotational flow motion theory (Rouse, 1938; Liggett, 1994), has been

previously reported by Marche *et al.* (1995), while similar findings were documented in undular hydraulic jumps (Montes and Chanson, 1998). Altogether, the results show very good agreement in both free-surface profiles and characteristic times for the simulation of the dam break on a wet bottom, compared to the analytical data. The numerical model gives very satisfactory results for this two-dimensional problem, as illustrated in this section.

Before considering 3D numerical simulations of positive surges in Sec. IV, we first propose in Secs. II E and III a fully detailed description and discussion of 2D validation test-cases of several methods to numerically generates proxy tidal bores.

E. Validation of a 2D positive surge generated by a fully closed gate (FC) compared to experimental data

As discussed in the introduction, many experiments found in the literature were performed for positive surges where the mean velocities V_b (fluid velocity flowing from downstream to upstream, when the tide rises upriver) and V_0 (river stream flowing downstream) are in the same direction and with $|V_b| < |V_0|$, thus corresponding to either FC (Fully Closed) or PC (Partially Closed) gate cases. This provides relevant test cases for simulations of positive surges. Here, we chose the experimental data set of Chanson (2009b; 2010b) with a FC case. Note that these data were not specifically made for the validation of simulations, and many required detailed needed to recreate the comparable simulation are not available, although this was one of the most complete where the bore is an experiment involving a fully closed gate experiment in a rectangular channel. For example, the experimental data for initial steady flow include only the discharge, and velocity and turbulence vertical profiles on the channel centerline at only one position. This would be insufficient to set the proper initial conditions to perform a 3D turbulent Navier–Stokes simulation. In the present comparison, the initial velocity is set to a constant velocity V_0 . With the Fully Closed (FC) gate cases, an analytical solution is available in terms of Fr , U_b , and V_b as long as d_0 and V_0 are known under the hypothesis of ideal fluid flow (Stoker, 1957; Henderson, 1966). Herein, the complete numerical domain consists of a vertical rectangle (Fig. 6) where the bore propagation takes place between $x = 0$ and $x = 10$ m. The domain is filled with water, initialized with the depth $d_0 = 0.199$ m and flow with a constant velocity $V_0 = -0.189$ m s^{-1} . The bore is generated by the impact of the flow against a fully closed vertical boundary, similarly to what is done in the experiment from Chanson (2010b). The 2D numerical domain is discretized into 5000×500 regular Cartesian mesh cells. The grid is evenly distributed in both longitudinal and

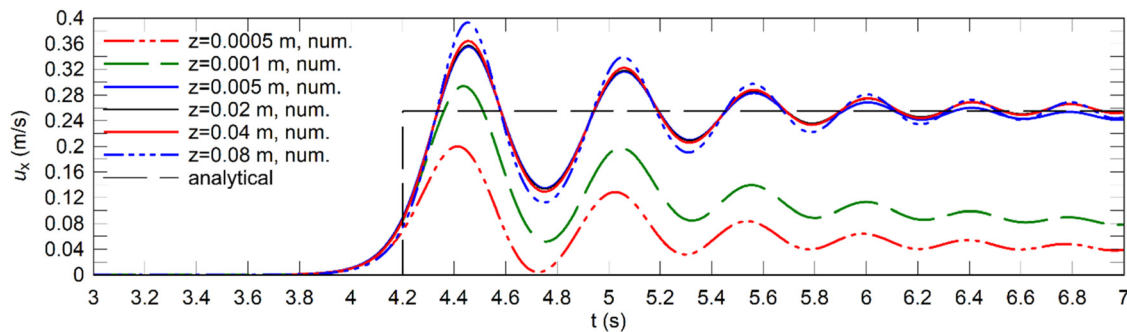
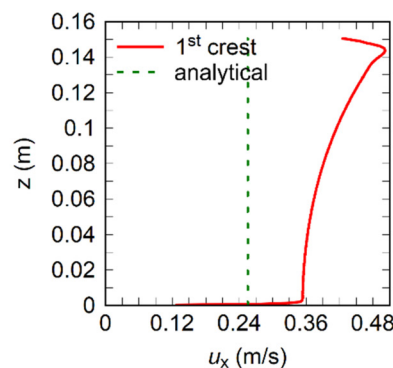
(a) Time evolution of u_x at $x = 5$ m, at several depths(b) Vertical profile of u_x

FIG. 9. Longitudinal velocity component underneath the undular waves generated by DB, (a) comparison between the numerical results (num.) and analytical formula (analytical). (b): vertical profile of the longitudinal velocity component directly under the bore front crest at $x = 4.125$ m.

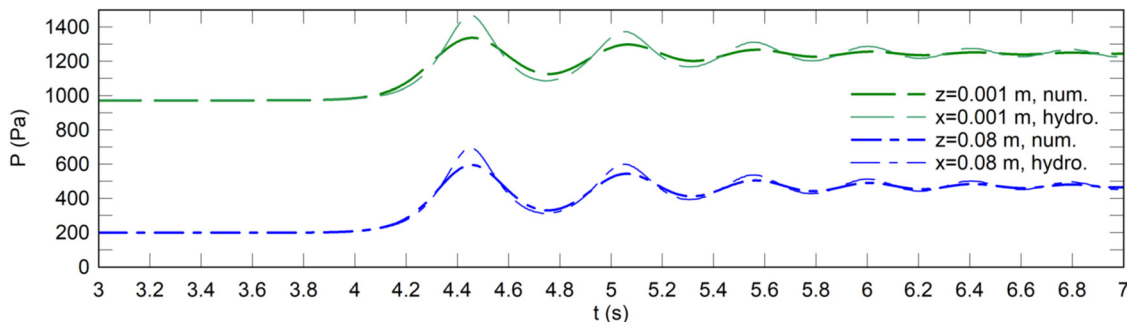


FIG. 10. DB case—Time evolution of the pressure at two elevations and $x = 5$ m. Comparison between the numerical results (num.) and hydrostatic pressure (hydro.).

vertical directions, giving a mesh grid resolution of $\Delta x = 2 \times 10^{-3}$ m and $\Delta z = 10^{-4}$ m. For the bore generation, the outflow boundary is closed with a no-slip boundary to emulate the rapid closure of the channel during the experiments. As the simulation starts, the flow impacts the boundary without splashing, creating an elevation of the water level propagating upstream and forming a bore with secondary undulations.

Figure 11(a) shows the dimensionless time evolution of the free surface at two locations, comparing numerical data and experimental measurements. The 2D numerical simulation reproduces closely the free surface evolution from the experiment. A direct comparison shows

that the bore conjugate depth, as well as first undulation maximum height, wavelength and first undulation minimum depth are within 3% differences with the experimental data. The amplitude is simulated within 15% from the experimental data, while the bore celerity differs by 2% (Simon, 2014).

Figure 11(b) shows the dimensionless velocity components measured at $x = 7.15$ m and $z = 0.146$ m deep. Both velocity components are compared to the experimental measurements, showing similar trends and evolutions as the bore propagates. The numerical results show again a good agreement with the experimental data, considering

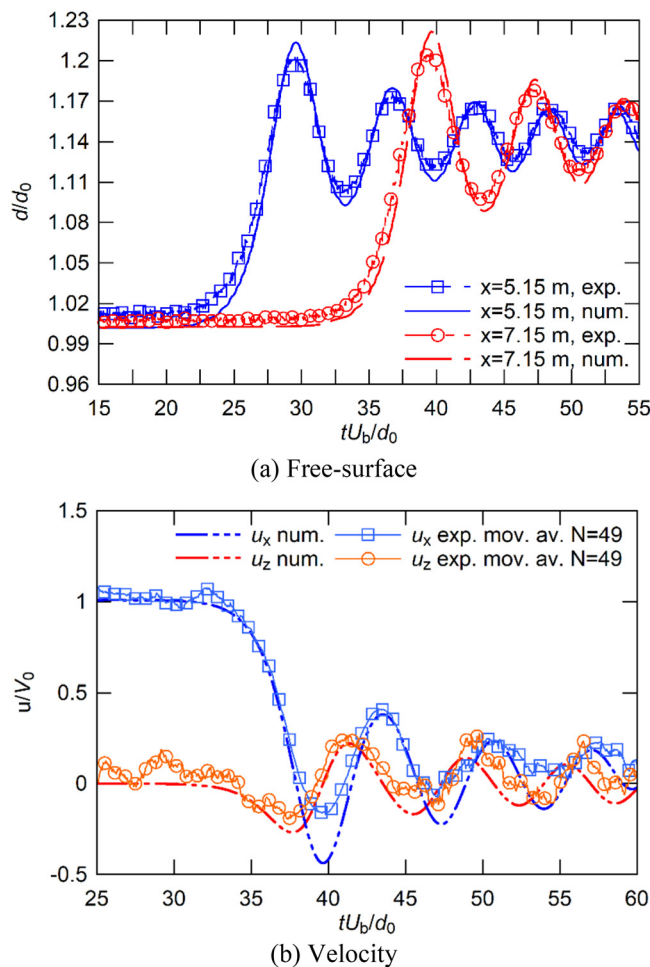


FIG. 11. FC case—Comparison between numerical (num.) and experimental (exp.) results. (a): non-dimensional time evolution of the free surface d/d_0 of undular bores. (b): non-dimensional time evolution of the dimensionless horizontal and vertical components of the flow velocity, u_x/V_0 and u_z/V_0 , at $z/d_0 = 0.73$ (where mov. av. = moving average and N = number of measured data).

the difference between experiment and simulated initial conditions, such as the turbulence (not taken into account in a 2D numerical simulation) and boundary layer development.

The validation tests covered several circumstances that lead to the formation of undular bores. However, the proposed model has proved the potential to simulate undular bores resulting from more varied mechanisms.

III. TWO-DIMENSIONAL BASIC FLOW FEATURES—COMPARISON AND DISCUSSION OF THE INITIAL SURGE GENERATION PROCEDURES

In this section, we first discuss on how to generate a bore. We used a 2D numerical domain with the flow conditions listed in Table II. We carefully compared the free-surface characteristics, and performed a thorough analysis of the hydrodynamics below the waves, considering undular bores and weakly breaking bores.

TABLE II. Numerical simulations initial parameters, $d_0 = 0.1$ m. The names of each simulations indicates the initial Froude number value, the type of initial flow configuration (DB stands for dam break, see Table I) and a number is given to distinguish bores of a similar type (OF1 and OF2, for example).

Fr	d_b (m)	Case	V_0 (m/s)	V_b (m/s)
1.1	0.1134	Fr1.1DB	0	0.1287
		Fr1.1OF1	-0.0429	0.0858
		Fr1.1OF2	-0.0858	0.0429
		Fr1.1FC	-0.1287	0
		Fr1.1PC1	-0.3465	-0.2178
		Fr1.1PC2	-0.5643	-0.4356
1.2	0.1269	Fr1.1PC3	-0.7821	-0.6534
		Fr1.2DB	0	0.2522
		Fr1.2OF1	-0.05	0.2022
		Fr1.2OF2	-0.2022	0.05
		Fr1.2FC	-0.2522	0
		Fr1.2PC1	-0.3022	-0.05
1.5	0.1679	Fr1.2PC2	-0.3522	-0.1
		Fr1.2PC3	-0.5522	-0.3
		Fr1.5DB	0	0.601
		Fr1.5OF1	-0.2003	0.4005
		Fr1.5OF2	-0.4005	0.2003
		Fr1.5OF3	-0.55	0.0508
		Fr1.5FC	-0.6008	0
		Fr1.5PC	-0.8978	-0.2970

Figure 12 presents the dimensionless time evolutions of the bore free surface profiles at different longitudinal locations for different Froude numbers. The simulation data from the numerical probes are nondimensionalized using the bore celerity U_b to synchronize the bore passage. All the free surface profiles can be observed to exhibit the same features. A characteristic, which is often measured in undular bores, is the bore front shape, characterized by the ratio between the amplitude and the wavelength (a_w/λ_w) (Chanson, 2010a; Simon, 2014; and Putra et al., 2019). Figure 13 presents comparisons of the bore's shape with experimental and theoretical data, considering different bore generation methods. When compared with a large number of data, the present numerical results agreed well with the plotted data, quantitatively as well as qualitatively. This was confirmed by Putra et al. (2019). In particular, the values remain between the curves given by the linear and cnoidal theories (Lemoine, 1948; Andersen, 1978). The main observed differences occur for cases Fr1.1PC2 and Fr1.2PC3, when $|V_0|$ increases and induces modifications in the overall hydrodynamics, as detailed, as detailed below.

The following analysis details the hydrodynamics in the nonmoving frame of reference. Figures 14–16 present streamlines and isolines in the nonmoving frame of reference that represent the fluid direction and $u_x = 0$, respectively. Three main behaviors of the flow can be summarized hereafter.

- Complete flow inversion: There is a complete flow inversion beneath the bore when the longitudinal velocity component u_x changes sign over the water column. During the bore front passage, u_x goes from V_0 to a positive value. Beneath the secondary

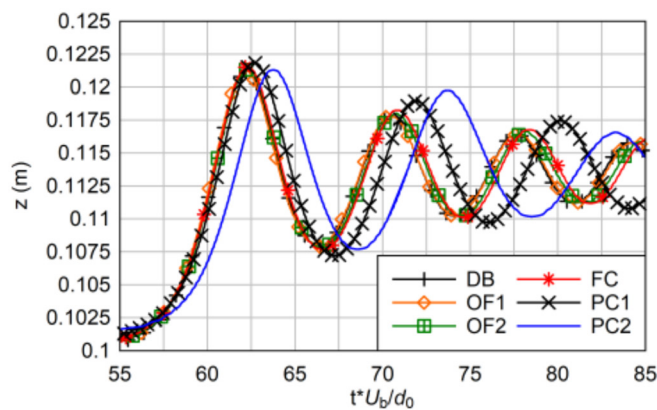
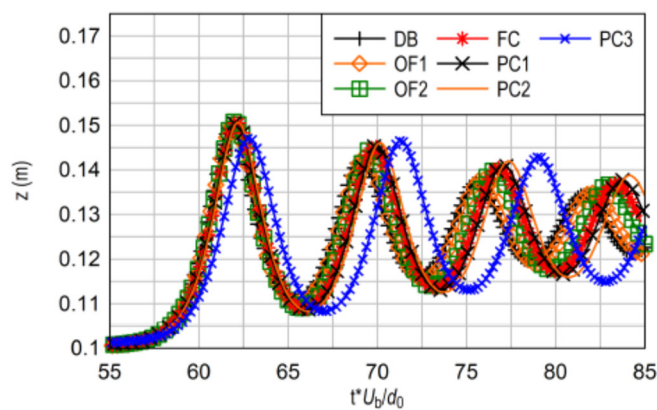
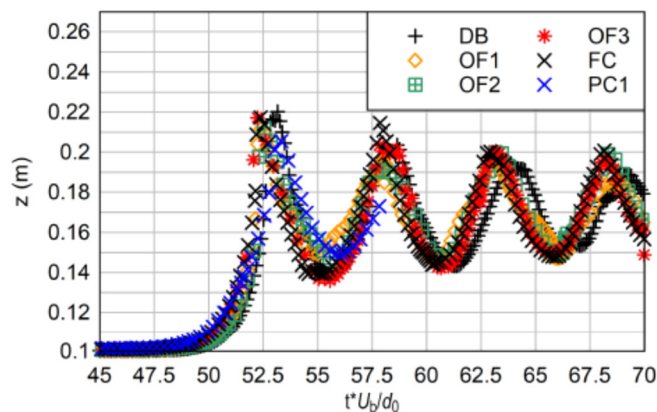
(a) cases $Fr = 1.1$, $x = 5.8$ m(b) cases $Fr = 1.2$, $x = 5.8$ m(c) cases $Fr = 1.5$, $x = 5.15$ m

FIG. 12. Comparison of dimensionless time evolutions of the free surface profiles, for the dam break (DB), opposing flow (OF), fully closed (FC) and partially closed gate (PC) bore generation method (see Table II). (a): cases with $Fr = 1.1$, at $x = 5.8$ m; (b): cases with $Fr = 1.2$, at $x = 5.8$ m; (c): cases with $Fr = 1.5$, at $x = 5.8$ m.

undulations, the velocity magnitudes oscillate around V_b in most of the water column and remains mainly positive. This happens for the DB [Figs. 14(a), 15(a), and 16(a)] and OF [Figs. 14(b)–14(d), 15(b)–15(d), and 16(b)–16(d)] Cases which exhibit a complete flow inversion, as seen with the black isolines at the inception of the bore front with the streamlines going in opposite directions from each part of the front.

- Alternating flow inversion beneath wave crests and troughs: there is a first inversion beneath the bore front with the flow going against V_0 . Beneath the secondary undulations, u_x is positive beneath the crest and negative beneath the trough over most of the water column. When the undulations pass, the u_x stabilizes around V_b (positive or negative). This happens for the OF [Figs. 14(b)–14(d), 15(b)–15(d), and 16(b)–16(d)], FC [Figs. 14(e), 15(e), and 16(e)] and PC [Figs. 14(f), 15(f), and 16(f)] cases. Note that for case $Fr1.2PC1$, the velocity only alternates under the bore front and the first undulation [Fig. 15(d)]. For $Fr1.2PC2$, the velocity does not alternate over the whole water column [Fig. 15(e)] but the dynamics is close to the other mentioned cases.
- No flow inversion: there is no complete change of direction of the current over the water column. The longitudinal velocity u_x remains in the same direction as V_0 in most of the water column and fluctuates around the value of V_b . There can be exceptions near the bed where intense flow reversal occurs under the wave crests. This happens for all PC cases.

Note that different hydrodynamics properties might be observed for breaking bores with no secondary undulations. Near the bed, velocity fluctuations and ejections of eddies could appear independently of complete flow reversal.

To summarize the observations detailed in this section, Fig. 17 presents three sketches outlining the flow hydrodynamics properties, in a nonmoving referential, encountered during this two-dimensional study. The discussion is mainly focused on the longitudinal velocity component u_x since the vertical velocity component u_z globally oscillates in relation to the free surface evolution, except when turbulence appears. In the tested configurations, three main situations appeared during the bore passage:

1. Figure 17(a): A complete flow reversal: u_x flows in opposite direction to the initial flow.
2. Figure 17(b): An oscillation of the flow: u_x oscillates under the wave crests of the secondary wave train.
3. Figure 17(c): No flow reversal: u_x mainly stays in the same direction as the initial flow.

Some distinctions are to be considered. In the upper part of the water column, for the second sketch presented in Fig. 17(b), the undulation of zone 1a does not necessarily start on the bore front. Flow reversal can remain unconnected (zone 1b) under the front and the first oscillations independently of the direction of V_b , as we can see in Fig. 16(d) with $V_b > 0$ and Fig. 15(e) with $V_b < 0$. Moreover, in the wake of the secondary wave train, the flow can either remain in the direction of V_0 or flow opposite to it. These situations are not necessarily linked with the changes appearing near the bed.

At the bottom, for every case except the DB, we observe a re-acceleration of u_x near the bed when wave crests pass [zone 2 in Figs. 16(b) or 15(c)]. It seems that zone 2 appears when $|V_0| \neq 0$. This

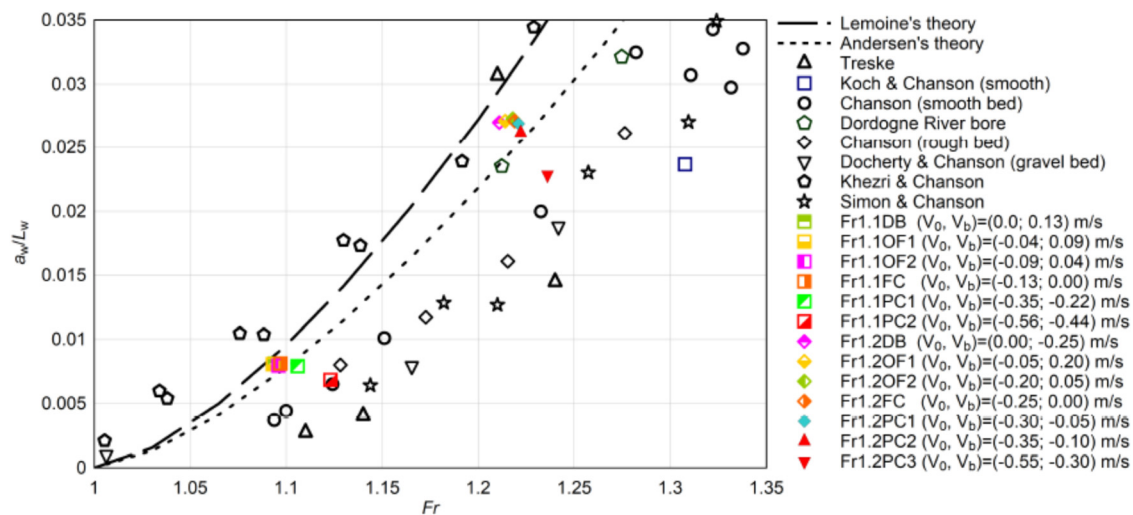


FIG. 13. Comparison of the bore front shape with data from theoretical and experimental studies. Linear wave theory (Lemoine, 1948), cnoidal wave theory (Andersen 1978), laboratory (Chanson, 2010a; Docherty and Chanson, 2012; Khezri and Chanson, 2012; Koch and Chanson, 2009; Treske, 1994; and Simon, 2014) and prototype (Navarre, 1995).

re-acceleration can be followed beneath the wave trough by a complete (zone 3a) or a partial (zone 3b) flow reversal [a good example for this can be seen in Figs. 15(c) or 15(d)]. The re-acceleration in zone 2 can also be followed by fluctuations and shedding of eddies moving upward (zone 4) as the flow is simulated with larger $|V_0|$ [Figs. 16(e) or 16(f)].

A change of bore shape together with the occurrence of fluctuations and ejections of eddies (zone 4) occurs in simulation with $|V_0| > 0.5\text{--}0.55\text{ m s}^{-1}$. For our cases, in which $d_0 = 0.1\text{ m}$, this corresponds to $Re > 5 \times 10^4$. In the literature, similar behavior for positive surges can be found in Lubin *et al.* (2010b), where the numerical results showed occurrences of large eddies for a simulated steady flow with $Re = 13.8 \times 10^4$ and a breaking bore with $Fr = 1.77$, while in Simon (2014), no eddies appeared for a simulated steady flow with $Re = 3.8 \times 10^4$ and an undular bore with $Fr = 1.14$, whereas eddies appeared for a simulated steady flow with $Re = 11.5 \times 10^4$ and an undular bore with $Fr = 1.25$. The dependency of eddy shedding with the Reynolds number should then be further studied to see if other parameters might change the threshold of Re around 5×10^4 , especially since the Reynolds number in rivers are often much larger. It may also occur as an interaction between the turbulent boundary layer developed in the river flow, which is not the subject of this study, and the bore front discontinuity propagating upstream. Nonetheless, turbulent behaviors are observed for the three Froude numbers used in this study as well as for other found in previous numerical studies. In summary, looking at bores in the frame of reference moving with V_0 and for a selected Froude number, the hydrodynamics behavior in bores changes when the Reynolds number of the steady flow becomes larger than a value close to 5×10^4 . Over that threshold, the hydrodynamics near the bed changes significantly with the occurrence of velocity fluctuations and the shedding of eddies, which propagate upwards in the water column eventually changing the shape of the free surface. This also showed that the Froude number is not a reliable indicator of the flow structure, especially near the bed. It may sound as an obvious

observation, as the Froude numbers are only related to free surface evolutions, but the striking feature shown in this study is that undular and weakly breaking bores defined for the same Froude numbers exhibit identical free surface evolutions, whereas the flow structures are different, as summarized previously in the three different scenarios sketched in Fig. 17. This means a great care must be taken when comparing laboratory or numerical studies to the natural flow. TBs are multi-parameters and complex problems that can hardly be decomposed into simple hydrodynamics features. In the future, simulations should be made for larger Froude and Reynolds numbers in order to further generalize our results, to study the interaction of strong wave breaking with eddies generated at the bed and to compare the effects for flow conditions closer to rivers. Tsunami bore conditions of occurrence also have to be analyzed at larger scales to get the complete understanding of the phenomenon (Bonneton *et al.*, 2016; Filippini *et al.*, 2019) and to better target the flow conditions to model.

IV. THREE-DIMENSIONAL VELOCITY FIELD AND TURBULENCE

A. Presentation

Based on the previous discussions and validations, we then propose to study the turbulent hydrodynamics under positive surges based upon three-dimensional numerical simulations. The numerical simulations were based on physical experimental data sets (Chanson, 2008; 2009b; 2010b; 2011b). The experiments were performed in a 12 m long 0.5 m wide rectangular flume. The bore propagated upstream against an initially steady open channel flow. The bore generation was controlled by the partial or complete closure of a downstream gate. Figure 19 illustrates the bore generation process in the numerical channel.

To numerically simulate bores, the experimental hydraulic channel was idealized into a rectangular numerical domain, which was a vertical rectangle for the two dimensional simulations and a cuboid for

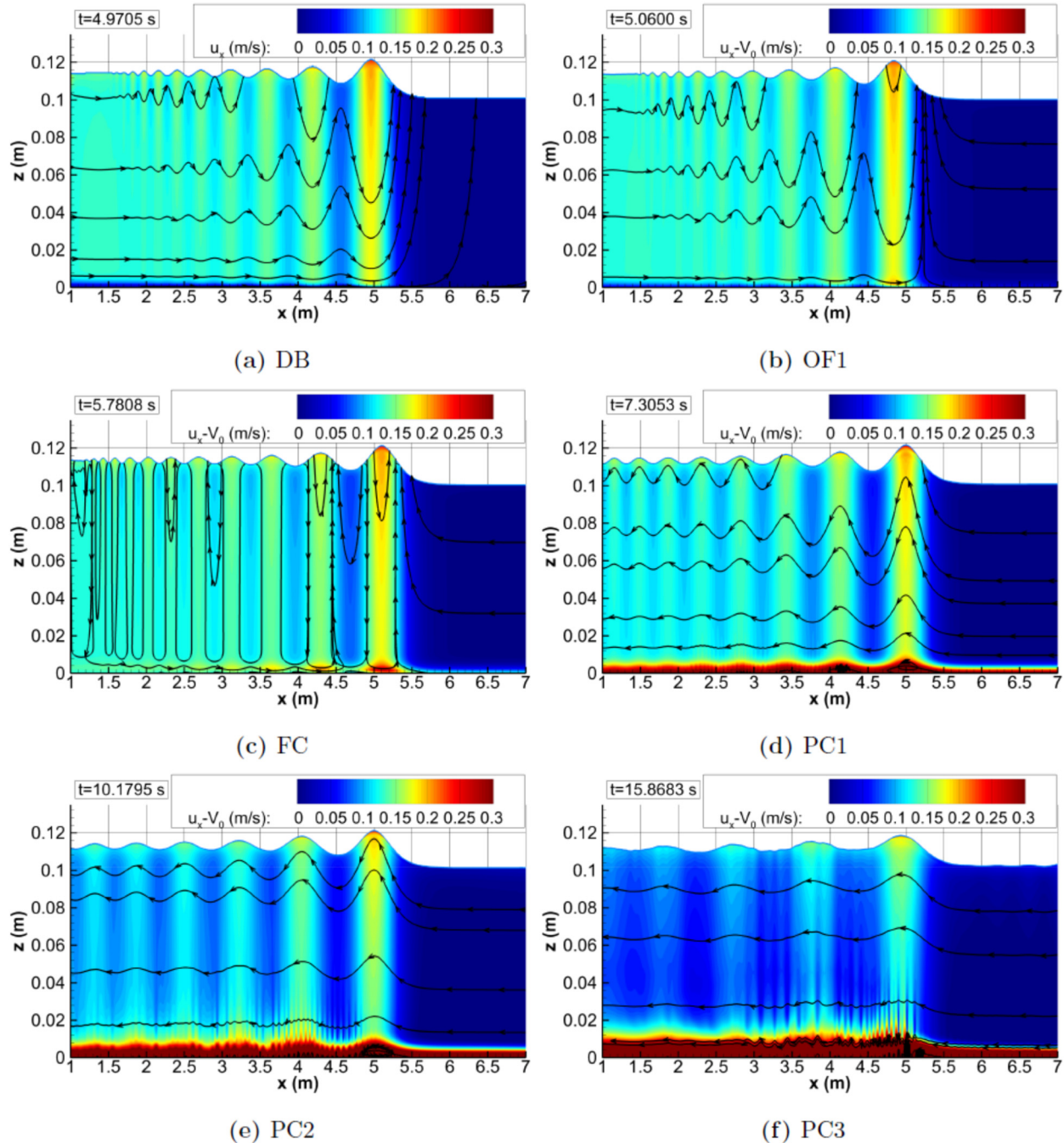


FIG. 14. Hydrodynamics of the undular bore for $Fr = 1.1$. The color maps show the longitudinal velocity component $u_x - V_0$ to simplify comparison between cases. The black lines are the isolines of $u_x = 0$ which show the flow reversal and recirculations (except for DB case, where V_0 is null). The arrowed lines show the streamlines presenting the direction of u at the presented time. (a): DB; (b): OF1; (c): FC; (d): PC1; (e): PC2; (f): PC3.

the three dimensional simulations. Before starting the 3D numerical simulations, the experimental steady flow conditions had to be recreated considering the SEM numerical procedure prescribed by Jarrin (2006; 2008). The numerical domain was filled with air and water,

with a constant water depth d_0 . The velocity of the water was set with a constant velocity V_0 . Both d_0 and V_0 were obtained from the experimental studies (Chanson, 2010b; 2011b). Then, the bore was experimentally generated by the fast closure of a gate (Fig. 18). For the

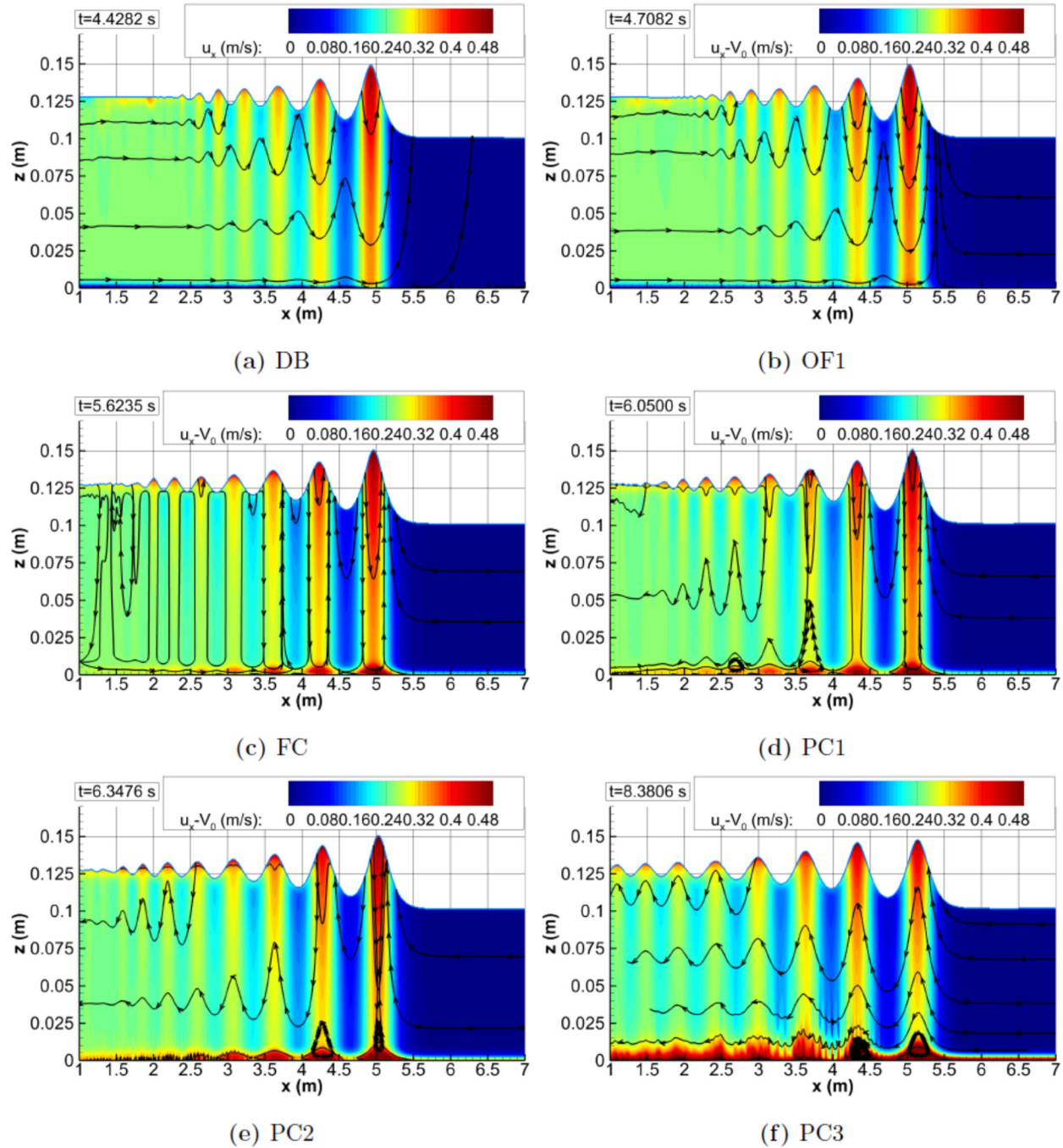


FIG. 15. Hydrodynamics of the undular bore for $Fr = 1.2$. The color maps show the longitudinal velocity component $u_x - V_0$ to simplify comparison between cases (except for DB case, where V_0 is null). The black lines are the isolines of $u_x = 0$ which show the flow reversal and recirculations. The arrowed lines show the streamlines presenting the direction of u at the presented time. (a): DB; (b): OF1; (c): FC; (d): PC1; (e): PC2; (f): PC3.

numerical simulations, the gate instantly appeared at the downstream end of the domain (Fig. 19), blocking the outgoing flow which then impacts a numerical wall. Table III presents the initial conditions used for the 3D numerical study. Only two experimental conditions were

selected for their completeness and similarity in Froude numbers (Table III). For each case, three simulations were performed: one 2D simulation, a 3D simulation with a constant uniform steady flow (i.e., $V_0 = \text{constant}$ in all the domain before the bore) and a 3D simulation

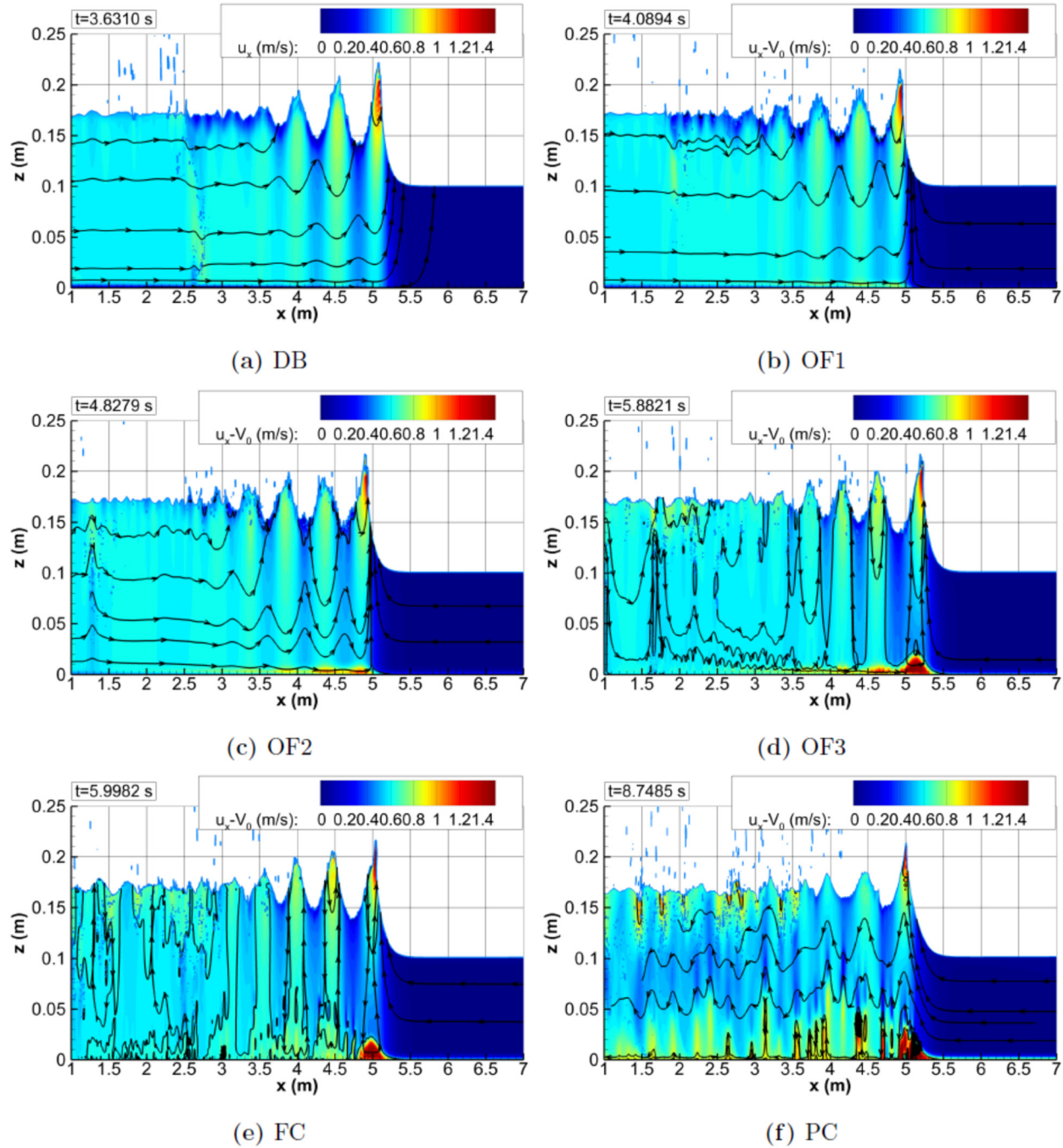


FIG. 16. Hydrodynamics of the weakly breaking bore for $Fr = 1.5$. The color maps show the longitudinal velocity component $u_x - V_0$ to simplify comparison between cases. The black lines are the isolines of $u_x = 0$ which show the flow reversal and recirculations. The arrowed lines show the streamlines presenting the direction of \mathbf{u} at the presented time. (a): DB; (b): OF1; (c): FC; (d): PC1; (e): PC2; (f): PC3.

with turbulent inflow condition (i.e., V_0 & SEM) (Table III). Each simulation adds a complexity to the problem during the bore propagation. That is, the 2D simulations overlook the three dimensional effects, and the 3D simulations without inflow turbulence ignore the effect of

inflow turbulence and turbulent boundary layer, present in the 3D simulations with SEM.

The numerical domain was 10 m long by 0.5 m high and for 3D simulations, and the channel was 0.5 m wide to match closely the

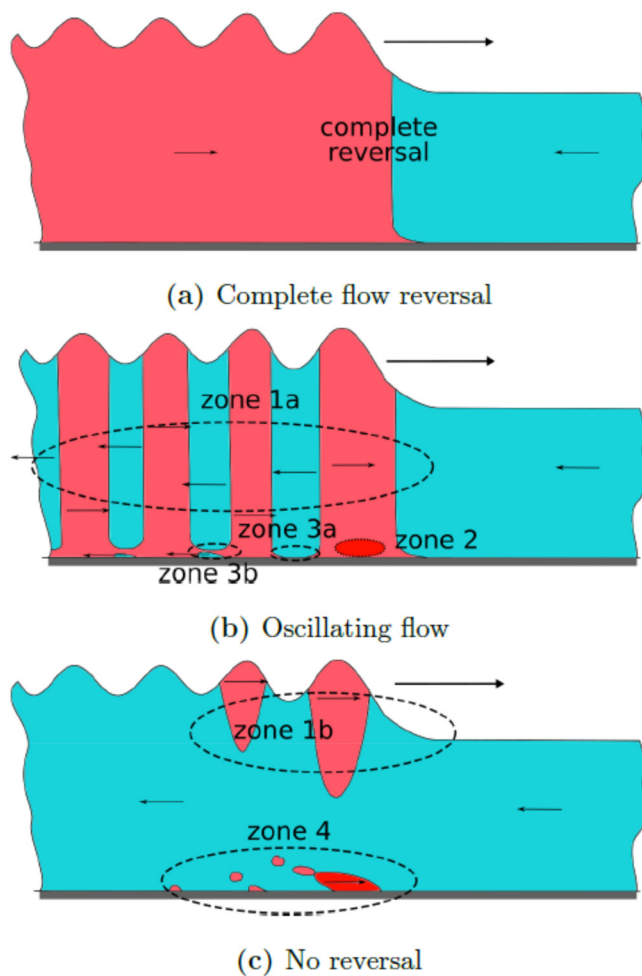


FIG. 17. Simplification of the hydrodynamics conditions appearing in positive surges. Scenario (a), (b), and (c).

experimental setup (Chanson, 2010b; 2011b). The numerical domain was slightly shorter than the experimental channel to save computing cost and to have the inflow condition generated by the SEM propagates on a smaller distance (Sec. II B). The domain was 0.5 m high to avoid

water from leaving the numerical domain through the top boundary during the splash happening when the flow runs up the downstream gate. The bed and lateral walls were set with a no-slip boundary.

Water and air filled the domain (Fig. 19). The viscosities of air and water were set as in the 2D validation section. The channel inflow continuously injected water between $z = 0$ and d_0 at a velocity V_0 in simulations with uniform inflow velocity (i.e., ond2D, rad2D, ond3D, and rad3D, see Table III). For the simulations with inflow turbulence (i.e., ond3DSEM and rad3DSEM, see Table III), a synthetic turbulent inflow condition (Sec. II B) was used at $x = 10$ m to recreate a turbulent boundary layer based upon the experimental observations on the channel centerline at $x = 7.2$ m upstream of the gate. For all the simulations, the remaining inflow condition was set with a no-slip boundary. The top of the domain was set with a Neumann condition and an absorption layer to control any spurious velocities. The absorption layer was a 0.15 m zone located beneath the top boundary with a smaller permeability than the air set to $K = 10^{-5} \text{ m}^2$. For 3D simulations with inflow turbulence (ond3DSEM and rad3DSEM), the outflow boundary at $x = 0$ m was set with a Neumann condition before the bore generation. In order to generate the bore, the outflow boundary was then closed between $z = h_g$ and 0.5 m with a no slip boundary keeping a Neumann condition between $z = 0$ m to h_g . The numerical details of the computations are summarized in Table IV, including the computational times.

1. Comparison with experimental results for the 3D numerical study

The steady flow conditions of the experiment were first reproduced in the simulation rad3DSEM using the SEM method configured with the mean and RMS velocity profile measured in the hydraulic channel (Chanson, 2011b). The flow was injected in the numerical domain with an average discharge of $0.0197 \text{ m}^3 \text{ s}^{-1}$ (Chanson, 2011b). Figure 20 presents dimensionless vertical profiles of the simulated steady flow conditions, in terms of mean longitudinal velocity and RMS velocity, compared to the experiment results (Chanson, 2011b). In the numerical simulation, the developing boundary layer presents a vertical profile for the longitudinal velocity similar to the one measured in the experiment, with an average error of 2.7%. However, the turbulent normal stresses were largely underestimated by the simulation (Fig. 20). This was expected since the simulations used experimental data measured at $x = 7.2$ m and injected the value at $x = 10$ m in the numerical domain, then compared again at 7.15 m, leading to some

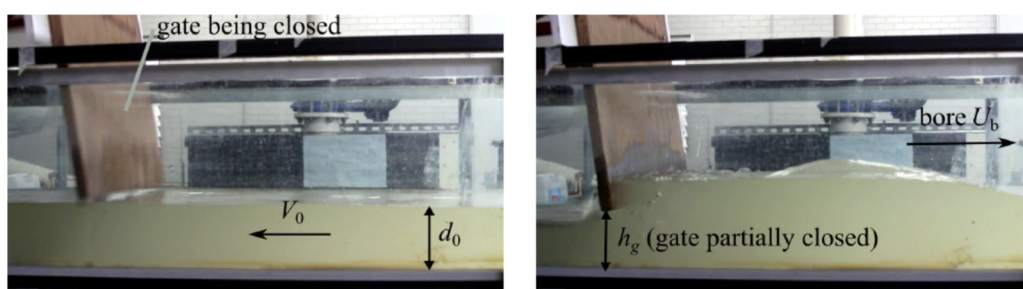


FIG. 18. Experimental generation of positive surge with a similar gate as in experiments (Chanson, 2010b; 2011b). On the left, the bore is not yet generated, the closing gate just hits the water free surface. As the tainter gate is partially closed (right), the undular bore appears and propagates against the steady flow (Photos: B. Simon).

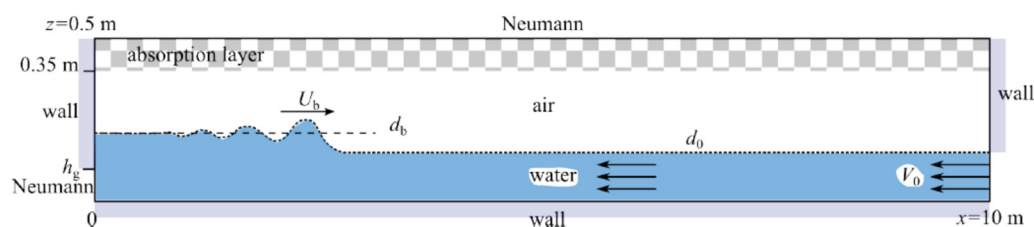


FIG. 19. 2D definition sketch of the numerical domain used for the simulations with the bore propagating in the 3D numerical domain.

TABLE III. List of numerical configurations used in the 3D numerical study, with their initial conditions and related experiments. ^aChanson (2010b); ^bChanson (2011b).

Computational configuration	d_0 (m)	V_0 (m s ⁻¹)	h_g (m)	Experimental run	Exp. Bore Froude Fr	Type of bore	2D/3D	Inflow turbulence
Ond2D	0.1385	−0.830	0.1	080 422 ^a	1.17	Undular	2D	No
Ond3D							3D	No
Ond3DSEM							3D	Yes
Rad2D	0.165	−0.230	0	090 427 ^b	1.13	Undular	2D	No
Rad3D							3D	No
Rad3DSEM							3D	Yes

TABLE IV. Details of the domain meshes and CPU requirements for the simulations made on supercomputers JADE at CINES for the 3D simulations (Intel® Xeon® E5450 4C 3 GHz) and AVAKAS in MCIA for the 2D simulations (Intel® Xeon® X5675 3.06 GHz).

Name	Number of meshes	Number of processors	Number of iterations	Consumed CPU time (h)	Physical time (s)
Ond2D	5000 × 500	36	300 000	1700	17.1
Ond3D	2000 × 250 × 100	640	80 000	184 000	13.2
Ond3DSEM	2000 × 250 × 100	640	95 000	245 000	23.2
Rad2D	5000 × 500	36	25 000	800	9.0
Rad3D	2000 × 250 × 100	640	45 000	46 000	8.8
Rad3DSEM	2000 × 250 × 100	640	60 000	230 000	39.4

discrepancies (Simon, 2014). Note that the value of the RMS for the experiments (Chanson, 2011b) were unusual and did not follow the classical decrease in the fluctuations with the distance from the bed as mentioned by Nezu and Nakagawa (1993) or measured in other experiments in hydraulic channel (Koch and Chanson, 2008; Chanson, 2010b). Nevertheless, the SEM method made it possible to obtain a turbulent steady flow, which was the main objective to this study.

a. Free-surface description. The bore’s free surface evolution and characteristics were calculated and compared to experimental measurements performed on the channel centerline at several distances from the gate (Chanson, 2011b). Figure 21 presents the dimensionless time evolution of the bore’s free surface at two distances from the gate when measured in the simulations, the experiment and calculated using Eqs. (1) and (2). Additionally, the bore celerity (U_b), wave amplitude (a_w), maximum water elevation (d_{max}) and wave period (T_w) of the bore are reported in Table V. In Fig. 21, the experimental data were synchronized with the numerical simulation at $x = 7.15$ m only,

as there was no recording of the exact instant of the manual gate closure.

The bore passage is characterized by a sudden evolution of the free surface followed by secondary undulations (Fig. 21). For the 3D simulations, the secondary undulations were mainly two dimensional with little variations in the transverse direction. The free-surface time evolutions are in good agreement between the numerical simulations, experiment and analytical values calculated with Eqs. (1) and (2). For both 3D simulations, the bore conjugated depth (d_b), the first undulation maximum (d_{max}) and the first undulation minimum (d_{min}) were within 2% of error with the experimental data, while both the wave period (T_w) and wave amplitude (a_w) were simulated within 9% of error from the experimental data. The bore celerity (U_b) was also within 1% of error as seen with the good synchronization of the bore propagation (Fig. 21). Overall, the simulation reproduced the free surface evolution with a very good agreement.

b. Velocity field evolution. Velocity data from the simulations were compared to the physical experimental measurements (Chanson, 2011b)

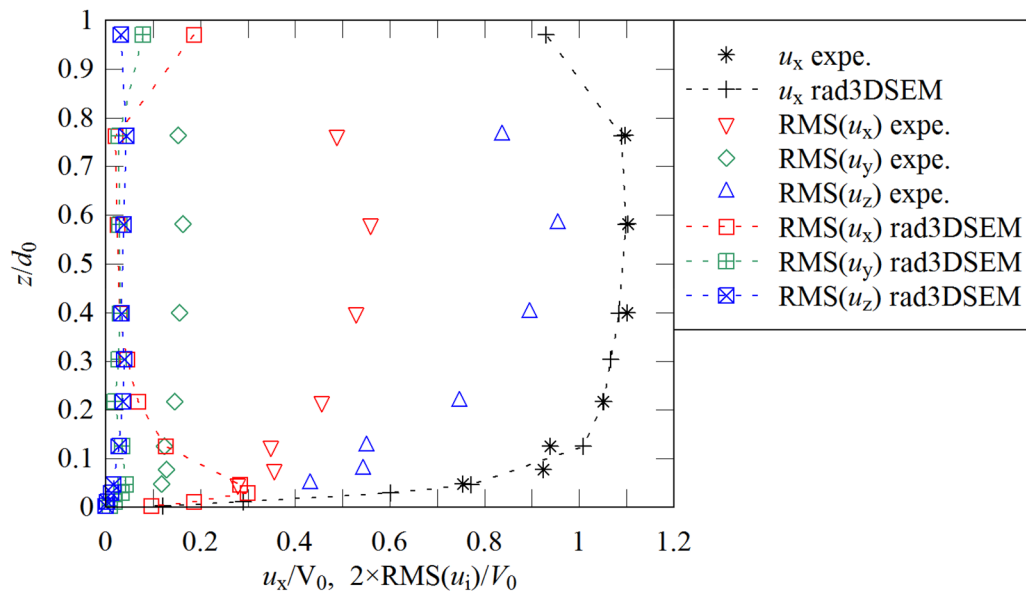


FIG. 20. Steady flow conditions. Dimensionless mean and RMS of the velocity signal generated using the SEM method (Jarrin, 2006; 2008) and measured in the experiment (Chanson, 2009b; 2011b). All data are measured at $x = 7.15$ m from the gate on the channel centerline and time averaged.

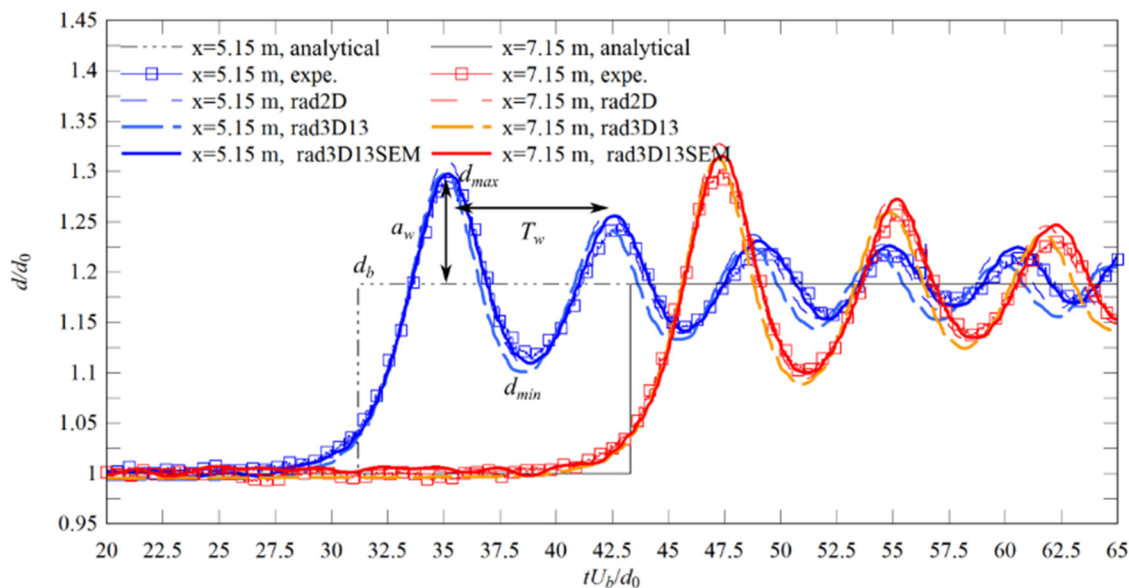


FIG. 21. Dimensionless free surface time evolution of the 2D and 3D undular bores. Comparison between numerical simulations, experimental data (Chanson, 2011b) (expe.) and Eqs. (1) and (2).

performed in the channel centerline at $x = 7.15$ m from the gate at several elevations using an Acoustic Doppler velocimetry (ADV) with single run measurements. Figure 22 presents the comparisons for the numerical and experimental data measured at $z \approx 0.036$ m. The experimental velocity measurements are presented with a moving average over 49 points (0.245 s) to display the data trend of the unfiltered

ADV signal that shows high frequency fluctuations and spikes. For completeness, these high-frequency fluctuations measured with the ADV are not necessarily representative of the turbulence. ADV signal outputs can record spikes (Cea et al., 2007) and finding the best filtering technique was not the objective here. Moreover, the ADV measures punctual data at 200 Hz whereas the simulation models the

TABLE V. Bore free surface patterns and characteristics for undular bores generated with a completely closed gate at $x = 7.15$ m (experimental run 090 427).

Results	Fr	U_b (m s ⁻¹)	d_0 (m)	d_b/d_0	d_{\max}/d_0	a_w/d_0	$T_w U_b/d_0$
Analytical solution	1.14	1.22	0.165	1.188
Experimental data (Chanson, 2011b)	1.13	1.21	0.165	1.200	1.303	0.103	8.067
2D simulation	1.14	1.23	0.165	1.206	1.327	0.115	7.901
Fr1.1FC							
3D simulation (no inflow turbulence)	1.14	1.22	0.165	1.176	1.312	0.112	7.634
Fr1.1FC3D							
3D simulation with inflow turbulence	1.15	1.22	0.165	1.194	1.315	0.107	7.321
Fr1.1FC3DSEM							

turbulence with a LES method which filters the turbulence in both space and time, hence the physical high frequency fluctuations cannot be represented by the LES in terms of time measurements.

For the longitudinal velocity component u_x , the numerical data and experiments showed a similar trend for the velocity evolution beneath the bore depending on the vertical elevation. For measurements at $z/d_0 = 0.12$ (see Simon and Chanson, 2013) beneath the first crest [Fig. 22(a)], the longitudinal velocity reached a value underestimated by approximately $0.16 \times V_0$ compared to the experimental data. For other elevations, the difference in velocity values was smaller than $0.1 \times V_0$. A similar evolution was observed beneath the following crests and troughs with a progressive de-synchronization of the crests and troughs with the experiment, as observed with the free surface measurements. Little differences were found between the two- and three dimensional simulations.

The transverse velocities u_y from the three dimensional simulations were compared to the experimental data. For the 3D simulation without inflow turbulence, the maximal variations were of magnitude $10^{-4} \times V_0$ [Fig. 22(b)]. No significant fluctuations of the transverse velocity were expected for this simulation since there was no initial turbulence in the flow and the data were measured in the channel centerline for an undular wave with a two-dimensional shape. The experimental data showed transverse velocity fluctuations of maximal magnitude up to $0.2 \times V_0$. For comparison, the transverse velocity fluctuations for the 3D simulation with inflow turbulence were approximately $0.05 \times V_0$ [Fig. 22(b)].

For both the numerical simulations and experiments, the vertical velocity component u_z is found positive and negative when the water level increases and decreases respectively. In agreement with the experiment [Fig. 22(c)], the vertical velocity oscillation magnitudes were the smallest close to the bed and the largest near the free surface.

Overall, the numerical results were in good agreement with the experimental results concerning both the free surface and the three velocity component trends on the channel centerline.

c. Comments on some limitations of the comparisons. The comparison between numerical simulation results and experimental data showed some limitations. The physical measurements were undertaken with an intrusive probe, i.e., an ADV, with a 1 cm diameter rod and a 5 cm head. Its effects on the flow cannot be dismissed (Simon and Chanson, 2013). Since the flow was simulated without the presence of an ADV, this resulted in an incomplete reproduction of the domain before bore generation. Future measurements with non-

intrusive probes, e.g., particle image velocimetry (PIV) and Laser Doppler velocimetry (LDV), could be beneficial including giving access to a mapping of the flow hydrodynamics (e.g., PIV), although the temporal resolution might not be the same.

Another shortcoming concerned the turbulent inflow conditions: the SEM created a different inflow condition than the experiment due to the interpolation of experimental data measured only in the channel centerline at $x = 7.2$ m and not in a whole channel transection. Since experimental data (i.e., mean and RMS flow velocities) were not available at the channel intake, we choose to use the SEM data measured at $x = 7.2$ m in the experiments and inject them in the numerical simulations in the inlet of the numerical domain ($x = 10$ m). This resulted in a turbulence magnitude underestimated due to SEM, as Jarrin (2008) reported a fast decay of the turbulence downstream the injection of the SEM data before it could reach a stable value. For a better modeling of the turbulence, the SEM should use data measured at the channel intake, when such data are available.

As for the comparison of the unsteady data between the experimental and numerical results, the experimental data were based on a single bore generation with measurements solely in the channel centerline. Comparison with ensemble statistics measured at several places across the channel would therefore be necessary to perform a more detailed validation of the simulations.

In conclusion, we choose to keep in mind one objective of the study, which is to compare the propagation of bore against a steady flow with and without turbulence, using the SEM method.

V. DISCUSSION ON 2D AND 3D RESULTS FOR UNDULAR BORES

The initial conditions of the simulation are chosen from physical experiments for their similar bore Froude numbers (Table I). A key difference is the value of V_0 and the global dynamics of the flow after the bore passage, i.e., the value V_b , if simplified as sketched in Fig. 3. For the case with the gate fully closed ($h_g = 0$), V_b is thus zero, whereas V_b is strictly negative when the gate is partially closed. In the following, the characteristics of the simulated bores are detailed and compared first by looking at the 2D, 3D, and 3DSEM numerical simulations with same initial velocities (V_0 ; V_b), then to one another.

A. Flow pattern under undular bores—fully closed gate (FC)

The results of simulations rad2D, rad3D and rad3DSEM (see Table III for the physical values and Table IV for the numerical details)

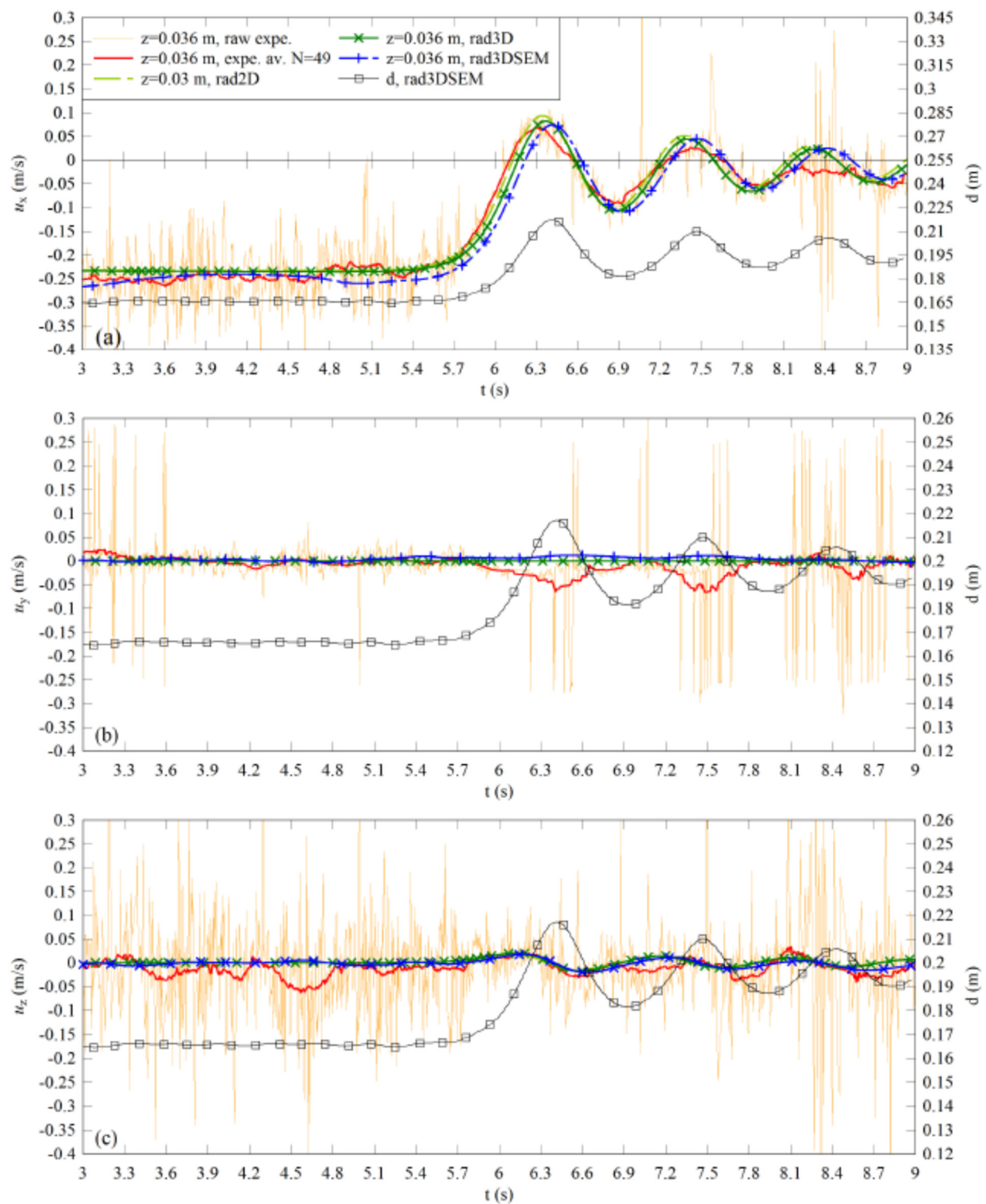


FIG. 22. Time evolutions of the velocity at $z \approx 0.036$ m with the free surface evolution at $x = 7.15$ m for rad2D, rad3D and rad3DSEM. Comparison between numerical simulations and experiments (Chanson, 2011b). Legend: "expe.": raw experimental data and "av. $N = 49$ ": moving mean of experimental data. (a) longitudinal, (b) transverse (no 2D data), and (c) vertical velocity components.

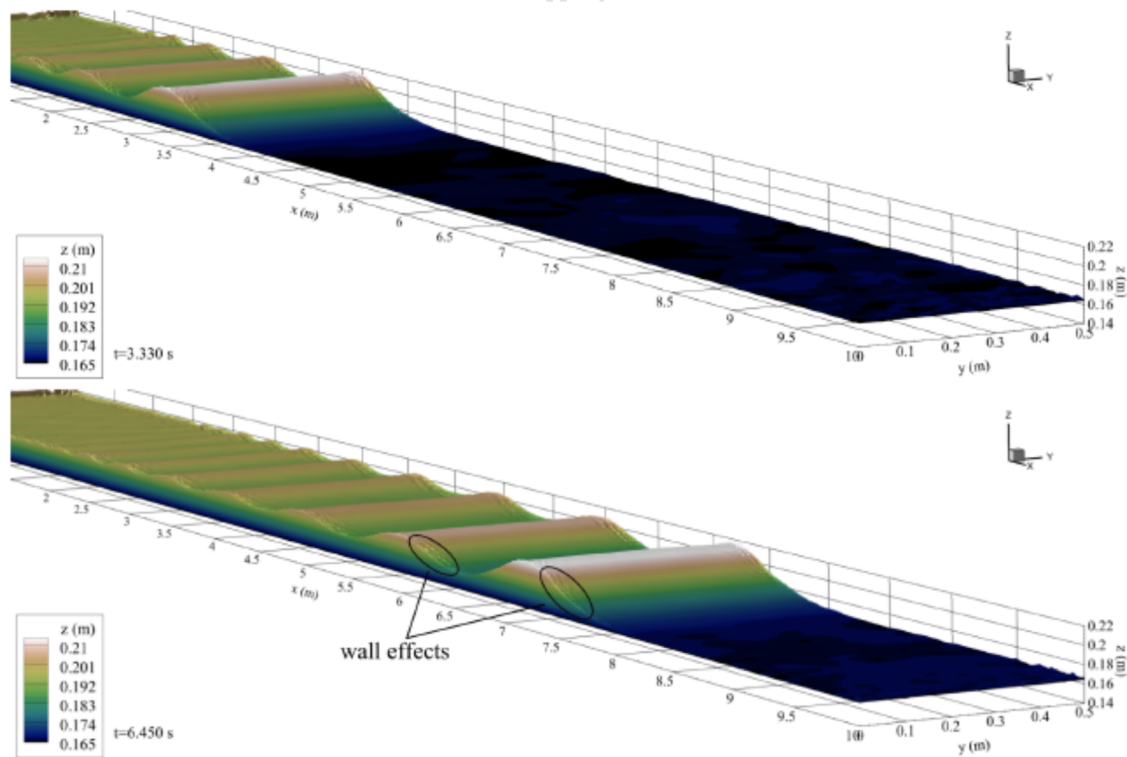


FIG. 23. Undular bore propagation illustrated by its free-surface elevation above d_0 for the simulation rad3DSEM at two different times. The color mapping on the free-surface indicates the elevation.

are discussed first. The propagation of the undular bore is illustrated by Fig. 23 showing, at two different times, contour maps of the free surface above d_0 for the 3D simulation with inflow turbulence (i.e., rad3DSEM). The flow properties together with the free surface are displayed for the 2D simulation (rad2D) in Fig. 24, for 3D simulation (rad3D) in Fig. 25 and for 3D simulation with inflow turbulence (rad3DSEM) in Fig. 26. In these figures, the zones of flow inversions are enclosed by the black isolines $u_x = 0$. Starting with the free surface evolution, the shapes of the bore's free surface for the two- and three-dimensional simulations were globally similar during the propagation which was coherent with experiments. At gate closure, the flow impacted the gate without splash. Within the first meter of

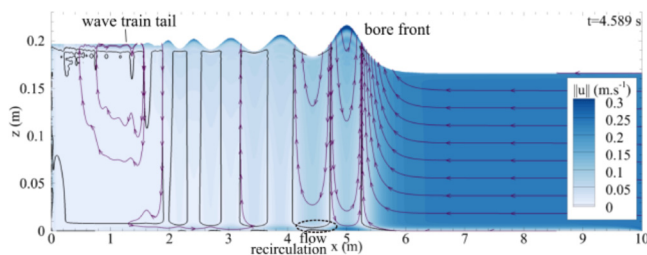
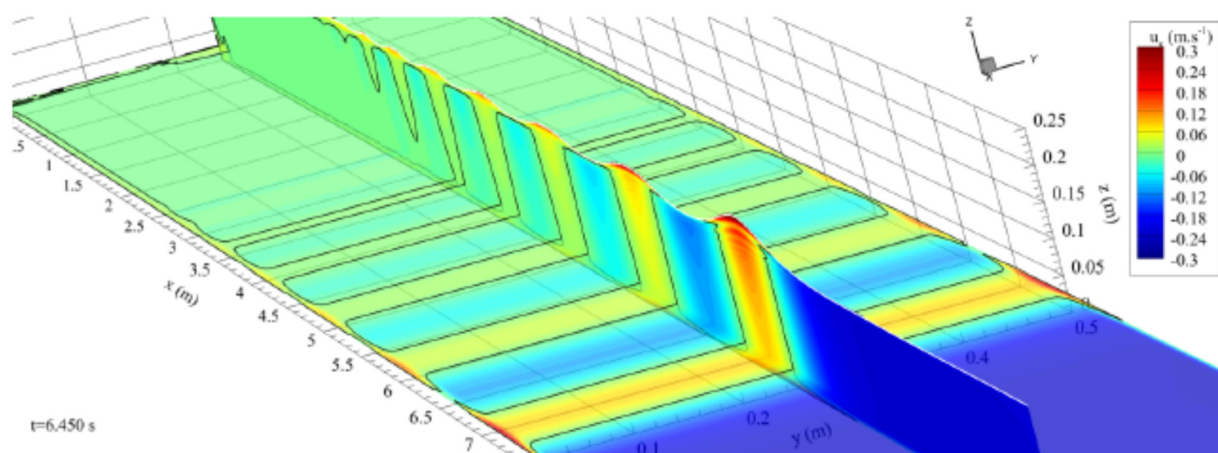


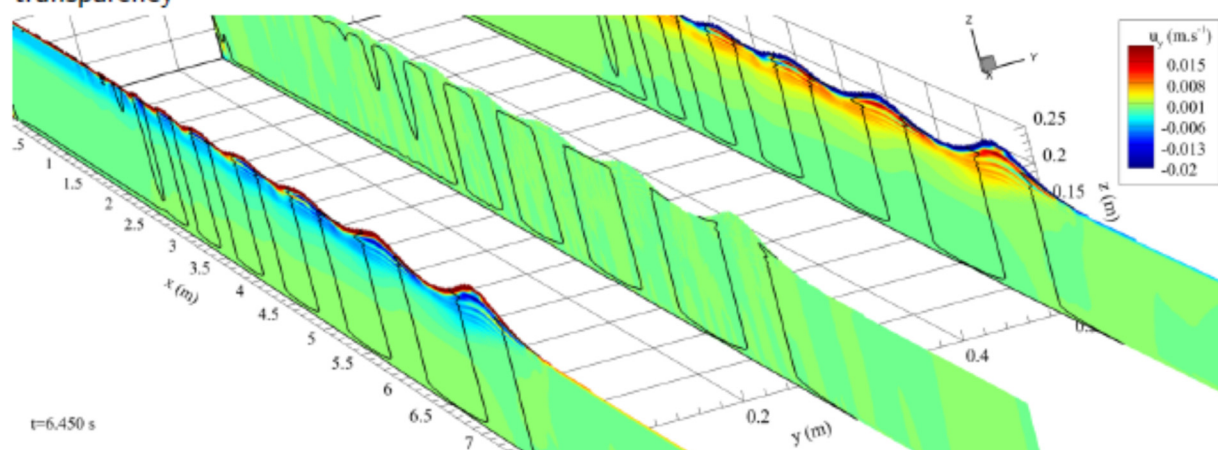
FIG. 24. Flow evolution beneath the undular bore rad2D. The color mapping represents the velocity magnitude with velocity streamlines (lines with arrows) and isolines $u_x = 0$ (black lines).

propagation, the bore quickly took the form of an undular bore followed by secondary undulations (Fig. 23). As the bore propagated, the bore front amplitude increased, while smaller undulations appeared one after another at the wave train tail. The amplitude and wavelength of the secondary undulations were decreasing from the undulations front to the tail (Figs. 23 and 24). Between the tail of the wave train and the gate ($x = 0$), the water level remained mostly unchanged during the entire bore propagation; the variations of the water level were smaller than the mesh size crossed by the air/water interface (at the interface $\Delta z \approx 1.1$ mm for rad2D and $\Delta z \approx 2.4$ mm for rad3D and rad3DSEM). Moreover, for the simulations, the bore conjugate depths d_b were similar to the experimental U_b and to the analytical value (see Table V). The use of the third dimension showed the apparition of small cross waves against the lateral walls initiated on the middle of the bore front (Fig. 23). Similar patterns were observed in the experiments, although not measured, and, for the simulation rad3D, the cross waves formed a 10.5° angle with the walls and approximately a 7° angle for simulation rad3DSEM. Overall, the three dimensional simulations are observed to keep a two dimensional aspect but allows a more realistic description of the free surface evolution, with three-dimensional features.

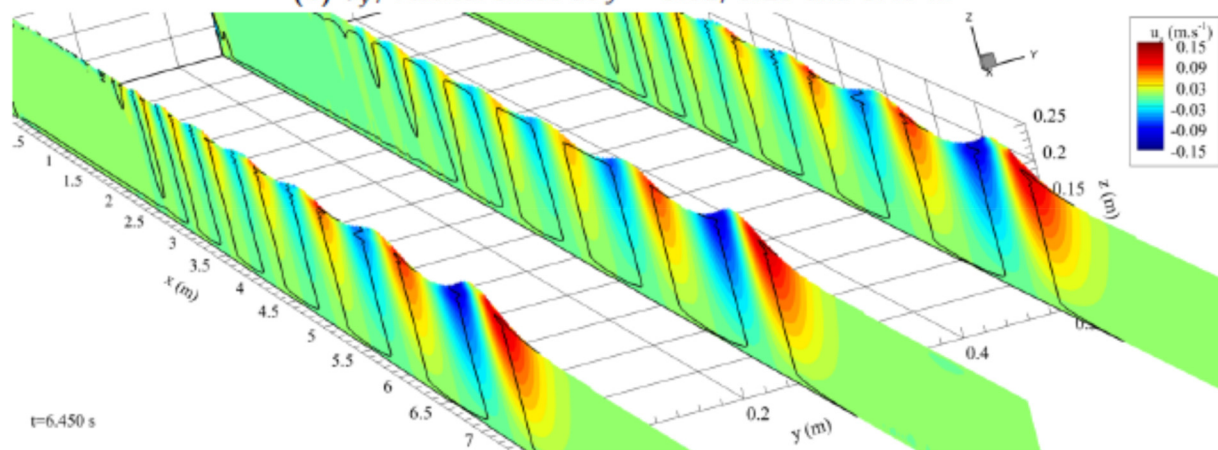
Focusing now on the velocity field, it closely followed the free surface evolution during the bore passage [Figs. 24, 25(a), and 26(a)]. As the water level oscillates, the longitudinal velocity alternatively decelerates and accelerates. Beneath the first crest, the longitudinal velocity changed direction flowing upstream on the entire water column



(a) u_x , vertical slice on the channel centreline and horizontal slice at $z = 0.025$ m plotted with transparency

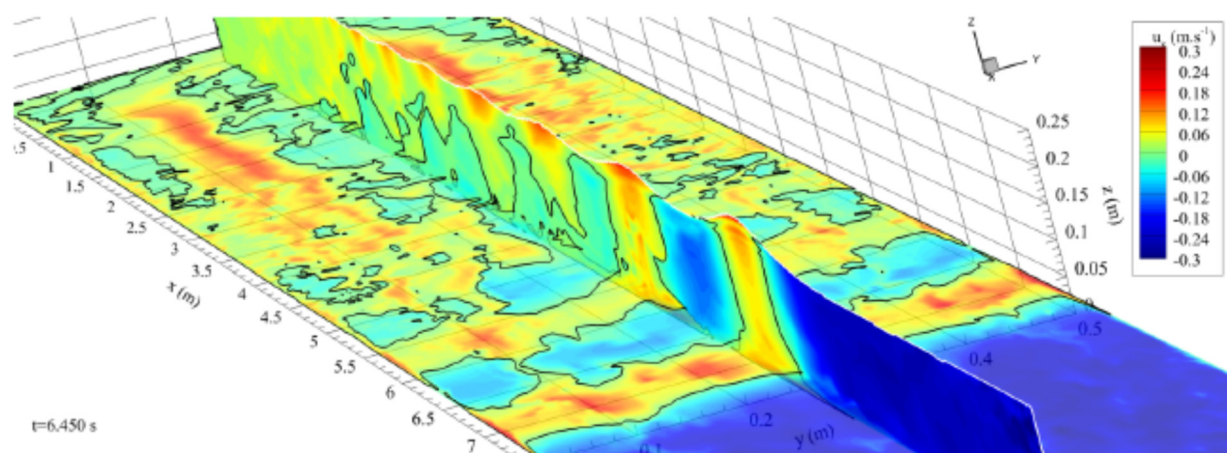


(b) u_y , vertical slices at $y = 0.01, 0.25$ and 0.49 m

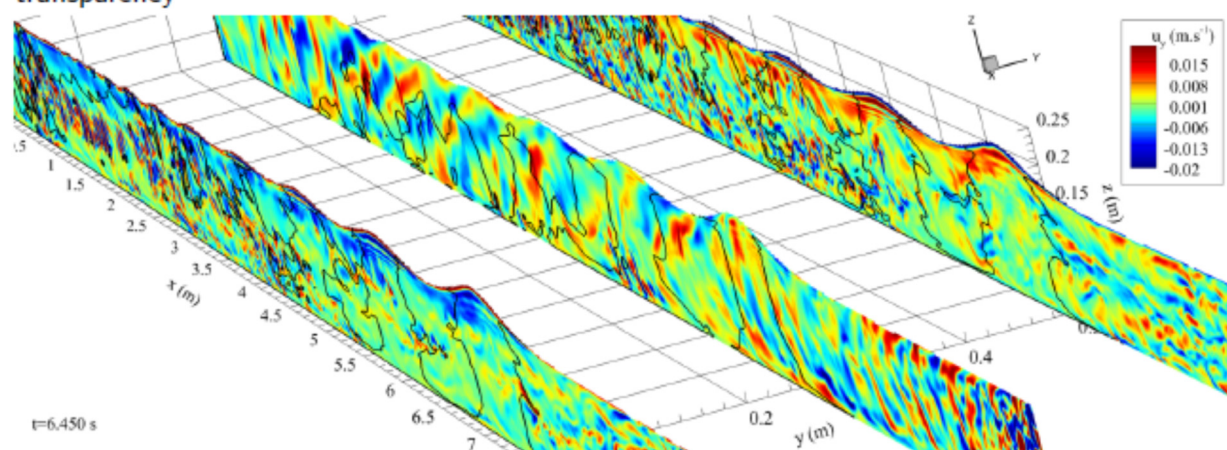


(c) u_z , vertical slices at $y = 0.01, 0.25$ and 0.49 m

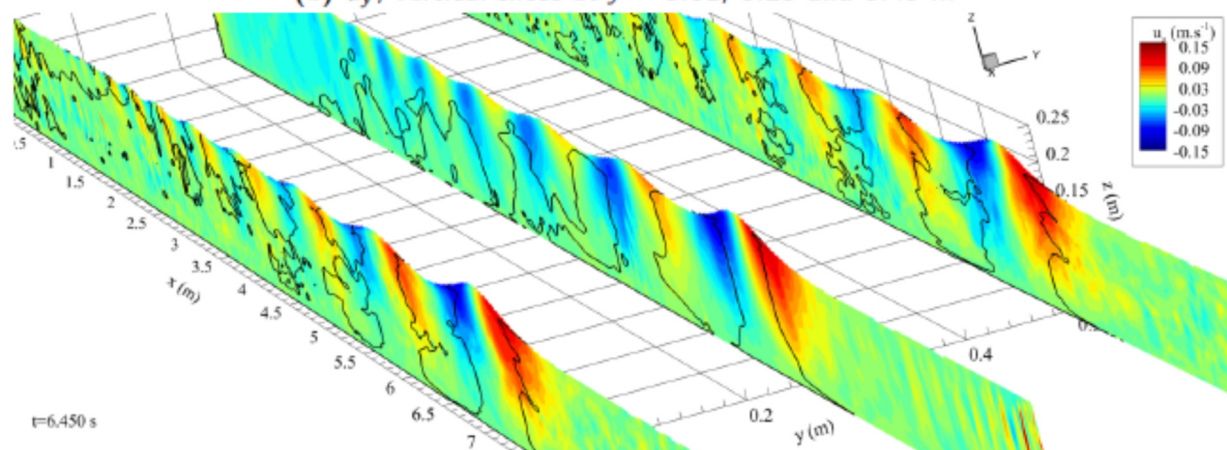
FIG. 25. Velocity fields in the undular bore rad3D as the bore propagates from left to right. The black lines represent the isolines $u_x = 0$. (a): horizontal component u_x ; (b): transverse component u_y ; (c): vertical component u_z .



(a) u_x , vertical slice on the channel centreline and horizontal slice at $z = 0.025$ m plotted with transparency



(b) u_y , vertical slices at $y = 0.01, 0.25$ and 0.49 m



(c) u_z , vertical slices at $y = 0.01, 0.25$ and 0.49 m

FIG. 26. Velocity fields in the undular bore rad3DSEM as the bore propagates from left to right. Black lines represent the isolines $u_x = 0$. (a): horizontal component u_x ; (b): transversal component u_y ; (c): vertical component u_z .

[contour line in Figs. 24, 25(a), and 26(a)]. Beneath the first wave trough, the flow direction changed again, flowing downstream except on a small zone. This zone was detached from the bed and located between $z \approx 1$ to 3 mm for rad2D, $z \approx 2$ to 4 mm for rad3D and appearing between $z \approx 0.5$ and 15 mm for rad3DSEM. Altogether, the zone of velocity reversal was observed close to the bed (dotted zone between $x = 4$ and 5 m in Fig. 24). Such a recirculation beneath the wave trough was not measured nor observed in experimental undular bores, probably due to the small height of the area and its proximity to the channel bed. Beneath the following secondary undulations, the longitudinal velocity followed a trend similar to the one observed beneath the first wave crest and trough with a longitudinal velocity flowing alternatively upstream and downstream but with a velocity range progressively decreasing [Figs. 24, 25(a), and 26(a)]. Nonetheless, after the second or third wave trough, the longitudinal velocity was oriented upstream a few millimeters beneath the free surface of the wave troughs [isoline $u_x = 0$ in Figs. 24, 25(a), and 26(a)].

The vertical velocity followed the evolution of the free surface as observed in previous physical studies (Chanson, 2011b; Simon and Chanson, 2013). The vertical velocity component u_z was globally positive and negative when the water level increased and decreased respectively [Figs. 24, 25(c), and 26(c)], i.e., the trend of u_z globally followed the time derivative of the free surface evolution as predicted by the ideal fluid flow theory. No fluctuation appeared for the 2D and 3D simulations (rad2D and rad3D) [Figs. 24 and 25(c)], whereas the 3D results with inflow turbulence presented fluctuations in both steady and unsteady flows (Fig. 26).

The transverse velocity component u_y was zero in most part of the domain for the 3D simulation rad3D except at the corner of the lateral walls and in the vicinity the bore's free surface [Fig. 25(b) slices 0.01 and 0.49 m]. For the 3D simulation with inflow turbulence (rad3DSEM), the velocity fluctuations during the unsteady flow remained within the same intensity range as for the steady flow (up to $0.05 \times V_0$) but covered wider areas beneath the bore [Fig. 26(b)].

Looking more into details at the flow evolution beneath the bore crest, strong flow reversals were observed close to the bed and near the free surface [Figs. 24, 25(a), and 26(a)]. At the flow interface of the bore crest, the flow reversal for u_x was up to $1.7 \times V_0$ for the 2D and 3D simulations, with larger values on the corner of the free-surface and the lateral walls [red zones in Figs. 25(a) and 26(a)]. Near the bed, a flow reversal with an intensity of 0.9 to $1.1 \times V_0$, with a variable height in the 3D simulation with inflow turbulence due to the turbulence in the steady flow [Figs. 24, 25(a), and 26(a)]. The flow reversal on the channel centerline of 2D simulation rad3D and 2D simulation rad2D were similar. The zone of flow reversal for the 3D simulation with inflow turbulence (rad3DSEM) was more irregular [black lines beneath crests in Figs. 25(a) and 26(a)]. Near the lateral wall, a strong flow reversal took place during the bore front passage at 3 mm from the walls. Below the other secondary oscillations, a similar pattern took place with velocity magnitudes progressively decreasing [Figs. 24, 25(a), and 26(a)].

The flow evolution between 3D simulations (rad3D and rad3DSEM) presented another difference: a zone of flow reversal was observed between the gate and the tail of the secondary undulations at a distance of approximately $3/10 \times W$ (with $W = 0.5$ m being the channel width) from both laterals walls, and beneath $z = 0.6$ m for 3D simulation rad3DSEM [between $x = 0$ and 3.5 m in Fig. 26(a)],

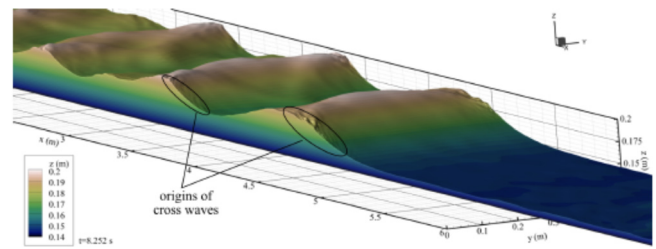


FIG. 27. Elevation of the free-surface for the simulation ond3DSEM with focus on the front between $x = 2$ and 6 m. The color mapping on the free-surface indicates the elevation and the bore propagates from left to right.

whereas the flow was mainly negative and two dimensional in the 3D simulation rad3D [Fig. 25(a)].

Overall, the flow evolution in the 2D simulation and on the channel centerline of 3D simulation without inflow turbulence presented similar flow characteristics. All the simulations, including 3D with inflow turbulence, showed zones of intense flow reversal taking place during the bore passage, beneath the wave crests. The 3D simulations gave access to the flow evolution near the wall, and the use of a turbulent inflow condition (i.e., rad3DSEM) allowed a more complete description of the unsteady flow motion.

B. Flow pattern—partially closed gate (PC)

The results of 2D and 3D simulations ond2D, ond3D and ond3DSEM (Table 1) are detailed here. Figure 27 presents the propagation of the undular bore for the 3D simulations with inflow turbulence at two different times by focusing on the free-surface. The flow evolution is displayed for the 2D simulation in Fig. 28, for 3D simulation in Fig. 29 and for 3D simulations with inflow turbulence in Fig. 30. The regions of flow reversal are enclosed by black isolines $u_x = 0$. The bore propagation in the simulations was similar to the experiments on positive surges (Chanson, 2010b). As the flow impacted the gate, a splash occurred with some air bubbles entrained below the gate. The water accumulating against the gate remained chaotic and bubbly during the first meter of propagation (Fig. 28). Then the unsteady free surface became smooth and propagated as an undular bore. As it propagated, more secondary undulations appeared. For three-dimensional simulations, small whirlpools appeared at the corners of the lateral walls and at the gate (mostly spinning with the centerline-gate-wall direction). The mean average water depth near the gate slightly increased by 2 to 3 cm as the bore propagated between 2 to 8 m from the gate. From a

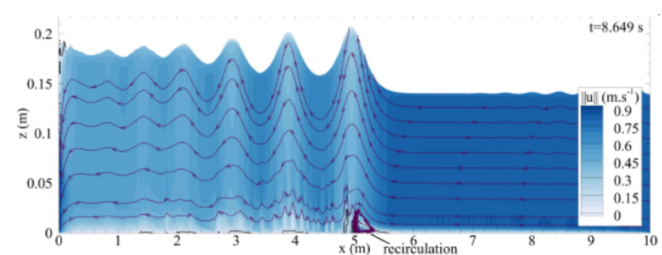


FIG. 28. Flow evolution beneath the undular bore ond2D. The color mapping represents the velocity magnitude with velocity streamlines (lines with arrows) and isolines $u_x = 0$ (black lines).

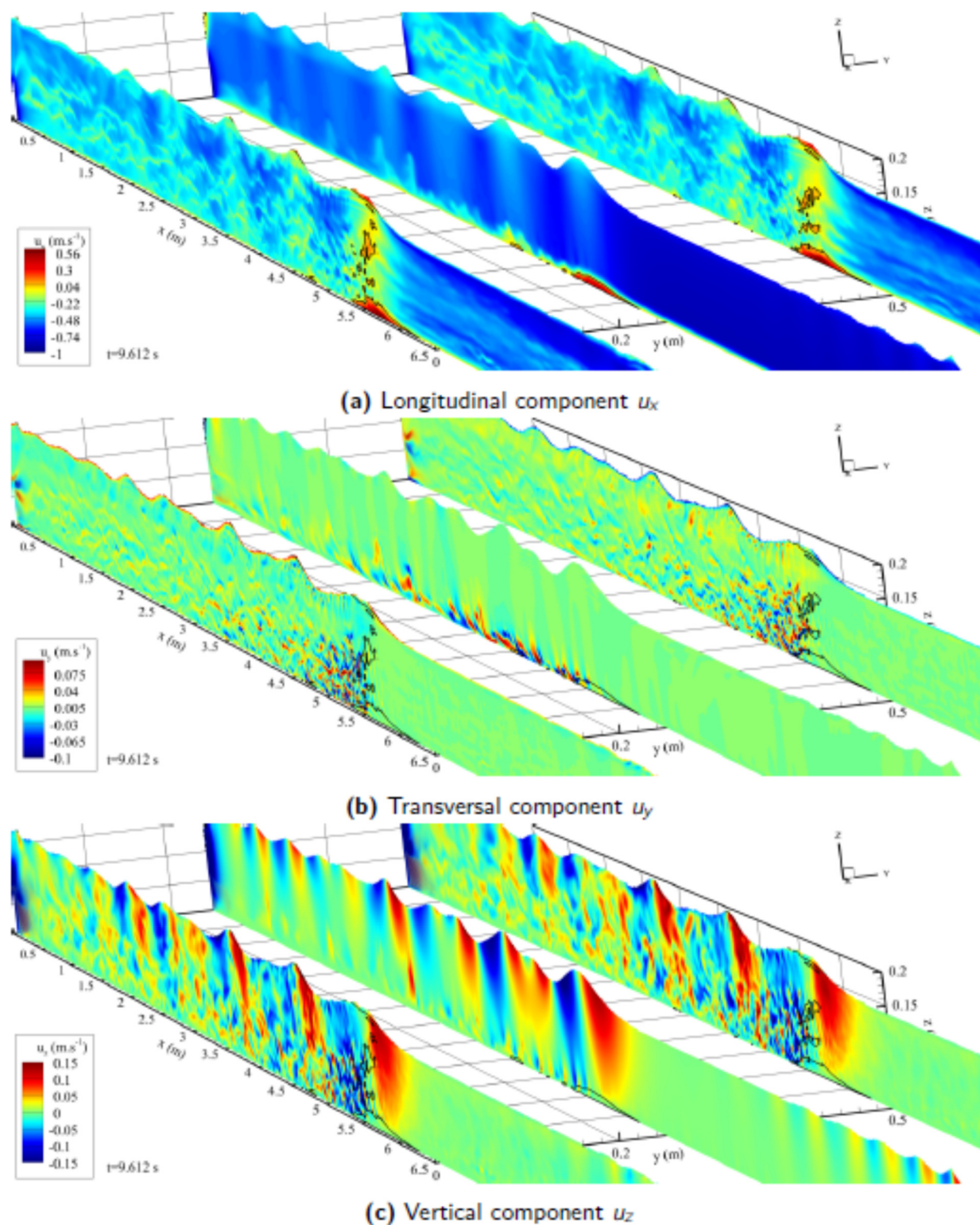


FIG. 29. Velocity fields in the undular bore on 3D as the bore propagates from left to right. Black lines represent the isolines $u_x = 0$. Slices on the channel centerline and 0.005 m from the lateral walls. (a): horizontal component u_x ; (b): transversal component u_y ; (c): vertical component u_z .

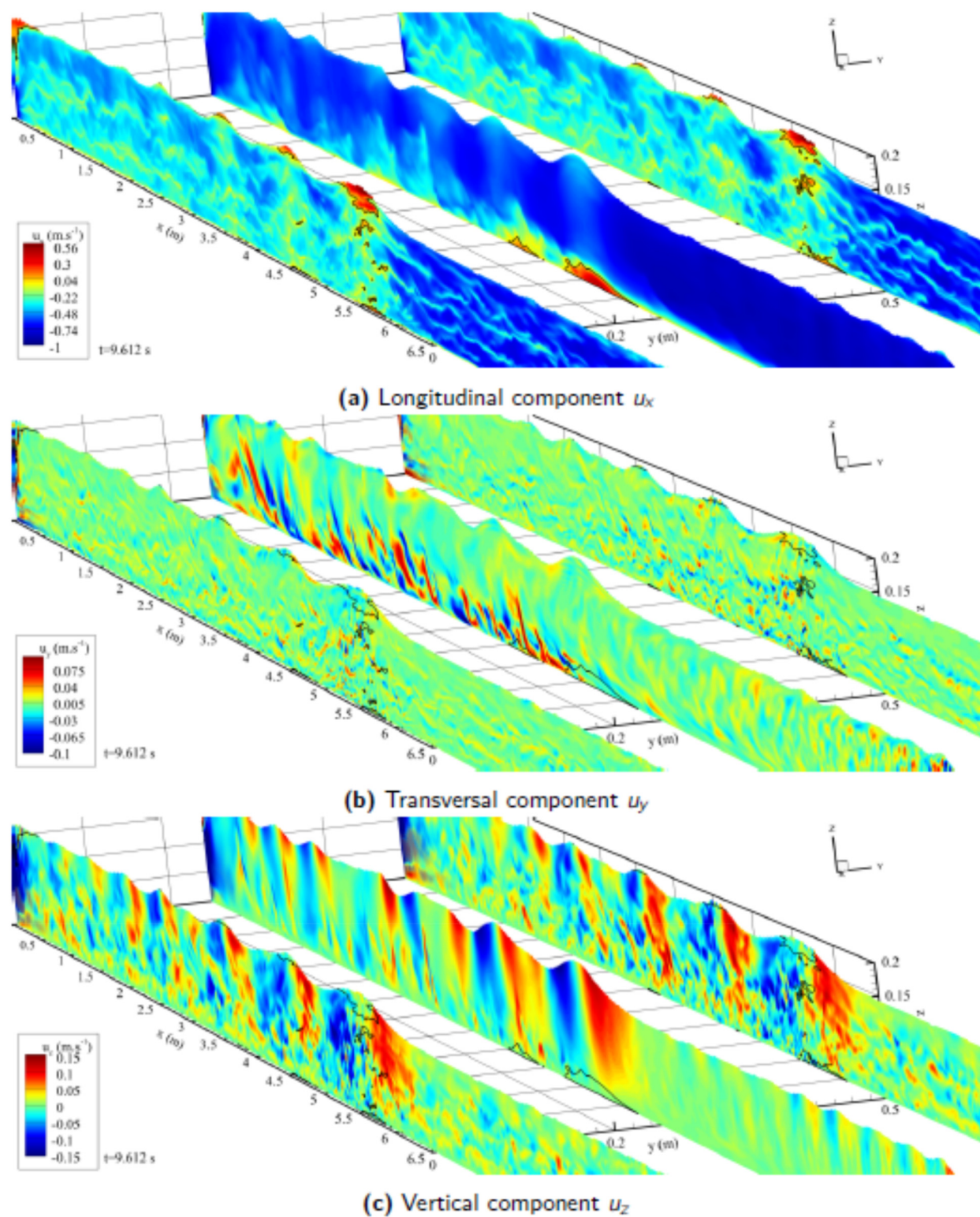


FIG. 30. Velocity fields in the undular bore on d3DEM as the bore propagates from left to right. The black lines represent the isolines $u_x = 0$. Slices on the channel centerline and 0.005 m from the lateral walls. (a): horizontal component u_x ; (b): transversal component u_y ; (c): vertical component u_z .

secondary undulation to another, both the wave amplitude and the wavelength decreased from front to wave tail (Figs. 27 and 28). The bores propagated at a celerity $U_b = 0.625 \text{ m s}^{-1}$ in 2D simulations (ond2D), 0.626 m s^{-1} in 2D simulations (ond3D) and 0.640 m s^{-1} in 3D simulations with inflow turbulence (ond3DSEM), with the bore Froude numbers of $Fr = 1.25$, $Fr = 125$, and $Fr = 1.27$, respectively. Hence, the bore propagated faster for 3D simulation case with inflow turbulence in the initially steady flow. The 3D simulations (ond3D and ond3DSEM) showed the presence of cross-waves at the bore front, similarly to physical observations (Montes and Chanson, 1998; Koch and Chanson, 2008). The cross-waves deformed the shape of the secondary undulations (Fig. 27) whereas the 2D simulation (ond2D) presented regular smooth shaped undulations (Fig. 28).

Overall, the three dimensional simulations presented a more complex free surface and velocity field than the two dimensional simulation for this set of initial configuration (d_0 , V_0 , h_g). The longitudinal velocity component u_x decelerated beneath the crests and re-accelerated beneath the troughs [Figs. 28, 29(a), and 30(a)]. Beneath the bore crest, the water continuously flowed downstream, except close to the bed: i.e., for $z < 20 \text{ mm}$ for ond2D, for $z < 15 \text{ mm}$ for ond3D and for $z < 35 \text{ mm}$ for ond3DSEM [Fig. 28 and red zones in Figs. 29(a) and 30(a)]. A flow reversal also took place within approximately 5 mm from the lateral walls. Beneath the first wave crest of the bore, the maximum velocity reversal in the recirculation reached up to $0.84 \times V_0$ ($u_x = 0.7 \text{ m s}^{-1}$) in the 2D simulation (ond2D), $0.54 \times V_0$ (0.45 m s^{-1}) for the 3D simulation (ond3D) and 0.48 to $0.72 \times V_0$ (0.4 – 0.6 m s^{-1}) in the 3D simulation with inflow turbulence (ond3DSEM). Similar recirculation was observed during experiments on undular bores (Ryabenko, 1998) and for breaking bores (Koch and Chanson, 2008), but not specifically for the experimental study (Chanson, 2010b) that the simulation configuration was chosen from. Downstream of the velocity reversal, the velocity fluctuations appeared in the 2D and 3D simulations. In addition to the flow reversal next the bed and walls, a strong flow deceleration took place 1 cm beneath the free-surface crest with the longitudinal velocity component u_x reaching $\approx 0.1 \text{ m s}^{-1}$. Note that the flow patterns were different from those in the FC simulations (rad2D/3D/3DSEM), where the longitudinal velocity completely changed direction between crests and troughs (Sec. V A).

In terms of the vertical velocity component, u_z was globally positive and negative as the water level increased and decreased respectively [Figs. 28, 29(c), and 30(c)]. Close to the bed, the fluctuations induced sporadic vertical velocity values down to $\approx 0.4 \text{ m s}^{-1}$ or up to 0.6 m s^{-1} (≈ 0.5 – $0.7 \times V_0$) for the 2D simulations (ond2D) and smaller values were reached $0.12 \times V_0$ for the 3D simulations (ond3D) ($\approx \pm 0.1 \text{ m s}^{-1}$) and $0.24 \times V_0$ for the 3D simulations with inflow turbulence (ond3DSEM) ($\approx \pm 0.2 \text{ m s}^{-1}$). It is conceivable that the 2D simulation overestimated the vertical velocity due to a two-dimensional confinement.

The transverse velocity component u_y in 3D simulations fluctuated largely after the bore passage particularly close to the bed and lateral walls, downstream of the longitudinal velocity reversal. For simulation with inflow turbulence (ond3DSEM), u_y fluctuated with values of magnitudes up to $0.1 \times V_0$ at a depth $z = 6.3 \text{ mm}$. Looking at the transverse velocity variations downstream the flow reversal, the successive positive and negative values of u_y indicated the generation of coherent structures which were smaller near the sidewalls than near the channel centerline [Figs. 29(b) and 30(b)].

Concerning the apparition of coherent structures near the bed, the 2D simulation (ond2D) presented velocity fluctuations with stronger intensity than the 3D simulations (ond3D and ond3DSEM). This could be an effect of the fluctuations developing only in a two dimensional domain. For the 3D simulations, the inflow turbulence in ond3DSEM seemed to have an effect on the flow velocity particularly beneath the bore front. The velocity fluctuations tended to move higher in the water column than in the absence of inflow turbulence. In the 3D simulation ond3D, the zone of flow reversal beneath the crest was mainly two dimensional over the channel width, whereas the flow reversal zone was strongly deformed by the initial turbulence for ond3DSEM.

Overall, the bore passage induced a strong flow reversal near the bed and generated fluctuations that were not observed in the bore presented in Sec. V A. For the 2D simulation, the intensity of the fluctuations was overestimated showing that three dimensional simulations were required. The use of the third dimension allowed modeling of the turbulence effects in the steady flow with the SEM. The steady flow turbulence might have an effect on bore celerity and induce a more turbulent flow after the bore passage. Moreover, the 3D simulations reproduced the effect of the cross-waves also observed in experiments.

C. Discussion on the turbulence in undular positive surges

Different inflow-bore interactions were observed depending on the flow conditions, i.e., the initial steady flow, with or without SEM addition, and the bore generation parameters, d_0 , V_0 , h_g . For the simulations ond2D/3D/SEM, a flow detachment was observed in the wake of the flow reversal near the bed, thus creating coherent turbulent structures, whereas, for the simulations rad2D/3D/SEM, a flow reversal occurred on the whole water column without the turbulent structures. For the simulation ond2D in particular, the coherent structures appeared with a frequency $f = 10.5 \text{ Hz}$ as the bore propagated. For the 3D simulations, a frequency could not be calculated since small structures appeared one next to the other toward the transverse direction and no distinct recurring pattern seemed to appear. An association of the shape of the zone of flow reversal, given by the black lines in Figs. 28, 25(a), and 26(a), could be made with bumps on a flat plate (Marquillie and Ehrenstein, 2003). The flow reversal zone created a downstream moving flow detachment similar to what can be observed in studies with a bump on a flat plate. However, for flow detachments downstream a bump, a reattachment of the flow occurs downstream the bump, whereas in positive surges, the generated detachments move upward in the water column, a motion possibly induced by the secondary undulations. The patterns observed for undular bores were also different than for the 2D case of breaking bore presented by LUBIN *et al.* (2010b). For the breaking bore, larger structures were formed near the bed, downstream the bore front and ejected in the flow. However, the simulation of the breaking bore was in two dimension and the present study showed large differences in velocity intensities in the ejected eddies between two dimensional and three dimensional simulations (cases ond2d and ond3d).

The use of the SEM showed that the initial steady flow turbulence was not responsible for the turbulence generated downstream the flow reversal. The apparition of coherent turbulent structures was rather a consequence of the choice of the flow conditions for which, in some simulations, a zone of flow reversal associated with a strong shear

appeared. For both cases, the Froude number was relatively similar (1.13 and 1.25), but the turbulent processes associated with the undular bore passage were completely different.

VI. DISCUSSION COMPARED TO RECENT RESULTS—CHALLENGES AND PERSPECTIVES TOWARD FULL SCALE NATURAL CONFIGURATIONS

Keylock (2005) discussed the potential applications of the LES for fluvial geomorphology studies and presented the large interest in accessing a lot of information for small details in the case of highly variable bathymetries, considering zones of different roughness, as well as configurations involving meanders or confluences, and even when dealing with the presence of hydraulic structures or obstacles is needed, numerical simulation provides information on the dynamics of large scales and their impact on suspension and sediment mixing.

Very recent experimental results, using non-intrusive experimental techniques, can be highlighted and compared to some of our conclusions. Lin *et al.* (2020a; 2020b) highlighted the complexity of surges due to dam-break generated undular bores, using high-speed particle image velocimetry (HSPIV) system. They confirmed our numerical results by reporting that the maximum and minimum values for the horizontal velocities were observed at the crest and trough phases, respectively, the vertical velocity profiles being almost zero. On the contrary, the maximum and minimum vertical velocities are observed at the ascent/descent phases. Thomas and David (2022) also used a non-intrusive experimental technique (particle image velocimetry—PIV). They studied an undulating bore, partially breaking at the leading wave. They noted that a significant effect was the thickening of the boundary layer after the jump front and observed a negative velocity under the jump. They were also able to identify vortices interacting with the roller front, these vortices would eventually descend into the main stream. They accelerate and small structures are invading the entire flow, establishing a connection with the boundary layer, confirming the potential of sediment suspension and advection when undular bores propagate upstream rivers. We were able to observe such a dynamic, as shown in Figs. 32(a) and 32(b), where coherent structures are observed to rise in the water column from the boundary layer, as the bore front propagates. Barranco and Liu (2021) also studied experimentally dam-break generated bores, using a high-speed particle image velocimetry system. They investigated the dependency of inundation depth, run-up height and flood duration on the reservoir length and the bore strength at the beach toe. They noted that the scale effects between large- and small-scale experiments are insignificant, due to Reynolds and Froude numbers consideration. They suggested that their results are thus applicable to “real world” conditions. Later, the same authors (Barranco and Liu, 2023) used a wave-maker to generated the bores and presented similar free-surface profiles and velocity field measurements than those discussed in the present study.

Whether the studies are carried out with physical modeling in laboratories or numerically, there will always be the question of representativeness, i.e., boundary conditions, validation, geometric assumptions, scale effects. Even *in situ* measurements suffer some limitations for generalization. As discussed in the introduction, field studies are often dependent on when the measurements are made (tide conditions, weather conditions, including rain and wind, sudden climatic events, floods, drought, etc.) or on the location (particular bathymetry, specific flow condition due to the presence of an island or a pontoon, etc.). Many technical limitations are also to be deployed, as it is

extremely rare to have access to all the planned instrumentation, or even to be able to deploy it adequately or effectively. It often happens that, on a scheduled survey, the planned data are also incomplete (failures, measurement interruptions, etc.).

Altogether, some questions need to be clarified concerning the characterization of the unsteady flow motion when looking at the field observations only: how can a tsunami-like bore (TB) be reproduced in laboratories to obtain an accurate physical modeling of the bore passage? What are the effects of the tidal rise, the estuary shape or the bathymetry on the bore which is only the front of the tide? Is there a unique simplification of the TB flow, and are all geophysical TBs comparable? Is it possible to simplify the natural flow as a physical model and is the outcome still comparable to the prototype flow? When modeling the general features of the flow, the initial and boundary conditions (geometric, kinematic and dynamics parameters) are of paramount importance, and their selection is governed by non-dimensional numbers ensuring analogy (complete or not). While Madsen *et al.* (2008) addressed some of these questions, turbulence was not taken in account in the discussion, so far.

However, it has to be emphasized that detailed numerical simulations of tidal bores in full scale rivers are not yet possible to perform for a study of flow turbulence. This is in part due to lack of data (such as detailed river bathymetry or complete flow hydrodynamics for the boundary and initial conditions to perform numerical simulations) and the numerical cost of such simulations. Bonneton *et al.* (2011a) experimentally showed, from field data, the significant cross-section variability of undular bores in contrast to what is observed in existing rectangular channel experiments, which has also been confirmed by Kobayashi and Uchida (2022) who showed the strong variability of the Froude number when bores are flowing through an experimental meandering channel, yet considering a constant cross section. Moreover, the parameters defining the intensity of a tidal bore can be complex, with rapid local variability (Bonneton *et al.*, 2015), but these parameters do not encompass the turbulent processes which are even more unsteady (not the same time and spatial scales of interest). As shown in this numerical study, similar Froude numbers can lead to some different turbulent flows, which is driven by the Reynolds number associated with local scales and may greatly vary all along the propagation of a bore upstream a river. Thus, numerical simulations of natural systems require the ability to model intricate domains such as open channels with curvature, sharp-bends and channel branching (Nachbin and Simoes, 2012), as well as non-uniform channels with arbitrary cross sections (Winckler and Liu, 2015; Kobayashi and Uchida, 2022).

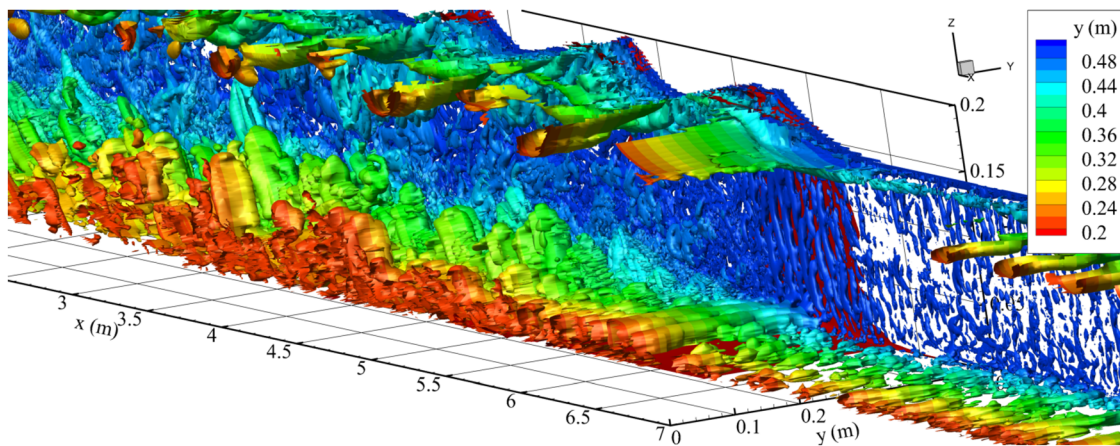
When an undular tsunami bores propagate upstream along an estuarine zone, the first few wave crests are much higher than the conjugate water elevation (Benjamin and Lighthill, 1954; Peregrine, 1966) and river bank overtopping and flooding may occur. The presence of secondary waves results in rapid and more frequent pressure fluctuations and higher loads on man-made structures such as bridge piers, jetty piers, and lock gates (Treske, 1994). In the case of navigation channels, ships and barges are adversely hindered during maneuver, as well as during loading/unloading of cargo. High mooring forces might result for ships breaking up their mooring, as well documented in the Qiantang and Seine Rivers (Malandain, 1988; Chanson, 2011).

However, even if full scale rivers are not yet possible to consider numerically, the consideration of more complicated geometrical

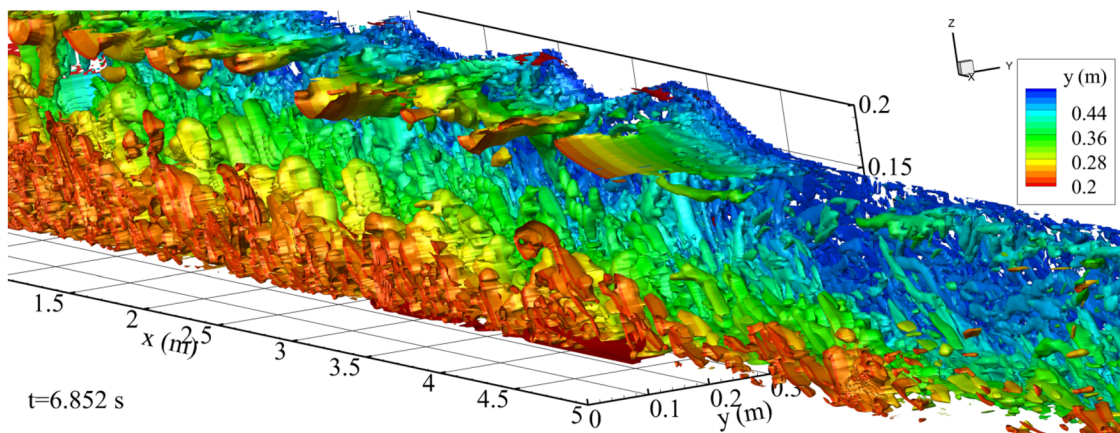
channel configurations is needed. In trapezoidal channels, the bore propagation becomes three-dimensional (Sandover and Zienkiewicz, 1957; Zienkiewicz and Sandover, 1957) (Fig. 31). The bore celerity is smaller, with a higher water surface elevation and “fishtail” waves (Benet and Cunge, 1971; Sandover and Taylor, 1962; and Violeau, 2022). The resulting effect is a lesser freeboard, with a higher risk of river bank overtopping (Treske, 1994) [Fig. 32(a)] and the drownings of individuals standing on the river banks, as well-documented in the Seine and Qiantang River (Malandain, 1988; Pan and Chanson, 2015). Physical measurements showed a complicated transient motion down the transverse slopes underneath the leading edge of the undular bore (Sandover and Taylor, 1962; and Kiri *et al.*, 2022a; 2020b). These studies highlighted a 3D unsteady flow motion, with an intense transient recirculation next to the invert at the base of the transverse slope and in the shallow flow zones, associated with intense secondary currents

on the transverse slope during a relatively short period corresponding to the passage of the bore front and secondary waves (Fernando *et al.*, 2020; Kiri *et al.*, 2020a) [Fig. 32(b)]. This was numerically confirmed by Chassagne *et al.* (2019).

Another major challenge concerns the aeration in bores. While the above development mostly focused on undular tsunami bore [Fig. 5(a)], a breaking tsunami bore is characterized by very turbulent transient front with a marked roller [Fig. 5(b)]. The strong turbulence induces rapid spatial and temporal deformations of the roller free-surface, in response to the dual-interactions between entrained air and vortical structures (Wüthrich *et al.*, 2021). Recent physical experiments showed large void fraction values in the bore’s leading edge (Leng, 2018; Leng and Chanson, 2019; and Shi *et al.*, 2023a; 2023b). The temporal evolution of vertical profiles of void fraction presented a rapid shift from convex to concave shape (Shi, 2022; Shi *et al.*, 2023b).



(a) Simulation Ond3D, Q-criterion plotted for $y > 0.2$, bore front located at $x = 5.7$ m, $t = 9.82$ s.

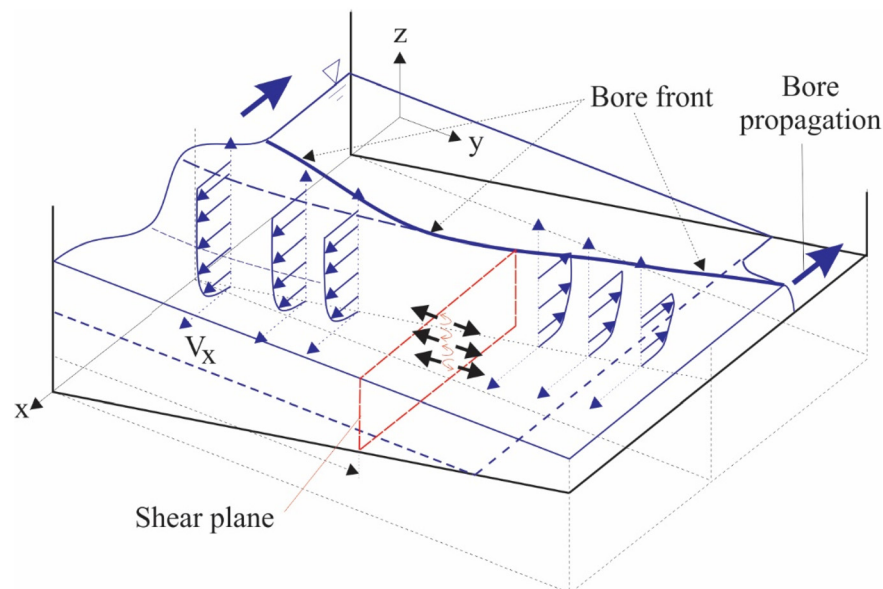


(b) Simulation ond3DSEM, Q-criterion plotted for $y > 0.2$, bore front located at $x = 4.5$ m, $t = 6.852$ s.

FIG. 31. Isosurface of the Q-criterion $Q = 2$ beneath bores with color mappings of the transversal distance and the isosurface of $u_x = 0$ in red. It can be clearly observed that the boundary layer tends to get thicker in the wake of the bore front. Numerical results taking the SEM into account shows more penetration of the eddies from the bottom to the core of the water column. (a) Simulation Ond3D; (b) simulation Ond3DSEM.



(a) Undular bore in the hydropower canal of Mallemort (France), looking at the incoming bore (Photo EDF)



(b) Schematic of transient velocity field on a sideslope of trapezoidal channel

FIG. 32. Bore front propagation in trapezoidal channel. (a): undular bore in France; (b): scheme showing the flow structure.

Depth-averaged void fractions across the roller height of 0.60 were recorded in breaking bore roller, followed by an exponential decay in mean void fraction with time (Chanson, 2022). The data implies a very rapid relative de-aeration of the roller region across the upper flow region.

The presence of air in the breaking bore is of significance for several physical processes, including the impact forces on man-made structures (e.g., bridges, jetties, groynes), the turbulent dissipation of bore energy as well as heat and mass exchange (e.g., marine aerosols) from free-surface water. Air entrainment, combined with debris transport and impact, will greatly affect the hydrodynamic loads estimation when a bore impacts dykes, or even buildings when overtopping occurs. Krautwald *et al.* (2022) described the importance to connect the knowledge of broken-bore flows to design non-elevated and

elevated coastal structures, and to deepen insight into forces, overturning moments and pressure distributions with a focus on the building's elevation above ground.

VII. CONCLUSION

The objective of this paper was to detail the complicated flow structure when undular bores propagate upstream a uniform flow in a rectangular channel.

We first compared and discussed the free-surface characteristics and the flow structures below the waves, considering undular bores and weakly breaking bores, using different methods to generate bores (dam-break, reflection wave due to an opposing flow, a partially closed gate, or a fully closed gate, hydraulic jump). A detailed study using various initial flow conditions (V_0 , V_b) was proposed to highlight the

limits and possibilities of the considered model. The discussion concerned mainly the longitudinal velocity component u_x which allowed to identify three scenarios:

1. A complete flow reversal, as the bore propagates upstream.
2. An oscillation of the longitudinal flow: u_x oscillates under the wave crests of the secondary wave train.
3. No flow reversal, with the longitudinal velocity remaining in the same direction as the initial flow.

The main finding was that, looking at bores in the frame of reference moving with V_0 and for a selected Froude number, the hydrodynamics behavior in bores changes when the Reynolds number of the steady flow becomes larger than a value close to 5×10^4 . Over that threshold, the hydrodynamics near the bed changes significantly with occurrence of fluctuations and shedding of eddies which propagate upward in the water columns. The most striking feature shown in this study is that undular and weakly breaking bores, defined for the same Froude numbers, exhibited identical free surface evolutions, but the flow structures were observed to be different, as summarized previously in the three different scenarios sketched in Fig. 17.

Then, the numerical simulations of undular bores were performed by solving the Navier–Stokes equations in two and three dimensions. Using physical laboratory data, unsteady inlet boundary conditions were reconstructed thanks to the SEM method. Although the turbulent flow conditions slightly differed, it is sought to be representative, considering the large CPU time cost. The simulations compared positive surges propagating against a turbulent and non-turbulent steady flow, in order to see the bore-turbulence interactions. The bore propagation against an adverse flow created a transient flow reversal next to the bed and lateral walls of the channel. The results show that the flow reversal and its turbulent wake differs depending upon the selection of initial turbulence conditions (SEM).

Then, the first 3D numerical simulations of undular bores were presented solving the Navier–Stokes equations. Two dimensional and three dimensional simulations were compared. Even though the 2D simulations followed the same trends as the 3D simulations, the complete detailed processes of bores could only be accurately represented by 3D simulations since the 2D simulations seemed to overestimate the velocity intensities in turbulent structures. Even if some limitations can be acknowledged, the flow conditions are considered to be in a reasonably good agreement. In particular, the capacity of the numerical model to reproduce cross-waves provides confidence in the numerical results. The use of inflow turbulence (SEM) showed the importance of the initially steady flow turbulence on the bore properties. The goal of this work was not to assess the best method for inlet turbulence generation, but rather to demonstrate the necessity to use turbulent inflow conditions and accurate thorough experimental data, if possible, when turbulence processes are targeted by the numerical simulations. This was confirmed by [Leng et al. \(2018\)](#) who showed, using the same numerical tool, the importance to ensure some in-depth knowledge of the physical model, including its characteristics (channel construction, gate closure mechanism and procedure, presence of joints or not, etc.) as well as its instrumentation (sizes and positioning, sampling frequencies, etc.). The CFD validation can be highly sensitive to any variations in the use of the experimental data.

Beneath the bore front, the flow velocity was observed to follow a similar evolution in all simulations. However, the flow below the

secondary undulations showed significant differences whether the steady flow turbulence was introduced or not.

The two different initial conditions (with or without SEM) tested herein also resulted in significantly different hydrodynamics processes during the bore propagation. This finding highlights the needs to define which experimental models are closer to geophysical tsunami-like bores, since the variations of the initial conditions induce drastic different unsteady flow evolutions. All the details presented, concerning the three-dimensional hydrodynamics of the flow in the whole water column beneath the bore front and the following wave train, are believed to be similar of tsunami-like bores, as discussed by [Madsen et al. \(2008\)](#). Altogether, the numerical simulations gave access to the 3D hydrodynamic details, which highlighted the possible knowledge that can be transferred to the study of the dynamics of tsunamis propagating in rivers. Numerical simulations can thus be used in complement to existing experimental studies.

ACKNOWLEDGMENTS

The authors wish to thank the Aquitaine Regional Council for the financial support towards a 512-processor cluster investment, located in the I2M laboratory. The first author was financially supported by the Aquitaine Regional Council and the University of Queensland. This work was granted access to the HPC resources of CINES, under allocation Grant No. 2013-x2012026104 made by GENCI (Grand Equipement National de Calcul Intensif), and the computing facilities MCIA (Mesocentre de Calcul Intensif Aquitain) of the Université de Bordeaux and of the Université de Pau et des Pays de l'Adour. The authors also acknowledge the financial assistance of the Agence Nationale de la Recherche (Project No. ANR MASCARET 10-BLAN-0911-01).

AUTHOR DECLARATIONS

Conflict of Interest

The authors have no conflicts to disclose.

Author Contributions

Bruno Simon: Formal analysis (equal); Investigation (equal); Methodology (equal); Software (equal); Writing – original draft (equal). **Pierre Lubin:** Funding acquisition (lead); Methodology (supporting); Supervision (equal); Writing – original draft (equal). **Hubert Chanson:** Conceptualization (equal); Formal analysis (equal); Investigation (equal); Supervision (equal); Writing – original draft (equal).

DATA AVAILABILITY

The data that support the findings of this study are available from the corresponding author upon reasonable request.

REFERENCES

- Abbott, M. B. and Rodenhuis, G. S., “A numerical simulation of the undular hydraulic jump,” *J. Hydraul. Res.* **10**(3), 239–257 (1972).
- Ai, C., Ma, Y., Ding, W., Xie, Z., and Dong, G., “An efficient three-dimensional non-hydrostatic model for undular bores in open channels,” *Phys. Fluids* **33**(12), 127111 (2021).
- Andersen, V., “Undular hydraulic jump,” *J. Hydraul. Div.* **104**(8), 1185–1188 (1978).

- Arnason, H., Petroff, C., and Yeh, H., "Tsunami bore impingement onto a vertical column," *J. Disaster Res.* **4**, 391–403 (2009).
- Bardina, J., Ferziger, J., and Reynolds, W. C., "Improved subgrid-scale models for large-eddy simulation," in *13th Fluid and Plasma Dynamics Conference, Fluid Dynamics and Co-Located Conferences* (American Institute of Aeronautics and Astronautics, 1980).
- Barranco, I. and Liu, P. L. F., "Run-up and inundation generated by non-decaying dam-break bores on a planar beach," *J. Fluid Mech.* **915**, A81 (2021).
- Barranco, I. and Liu, P. L. F., "Inundation, runup and flow velocity of wavemaker generated bores on a planar beach," *J. Fluid Mech.* **959**, A5 (2023).
- Barre de Saint Venant, A., "Théorie et équations générales du mouvement non permanent des eaux courantes," *C. R. Séances Acad. Sci.* **73**, 147–154 (1871).
- Bartsch-Winkler, S. and Lynch, D. K., "Catalog of worldwide tidal bore occurrences and characteristics," USGS Numbered Series Ci No. 1022 (U.S. Government Printing Office, 1988).
- Berchet, A., Simon, B., Beaudoin, A., Lubin, P., Rousseaux, G., and Huberson, S., "Flow fields and particle trajectories beneath a tidal bore: A numerical study," *Int. J. Sediment Res.* **33**, 351–370 (2018).
- Benet, F. and Cunge, J. A., "Analysis of experiments on secondary undulations caused by surge waves in trapezoidal channels," *J. Hydraul. Res.* **9**(11), 11–33 (1971).
- Benjamin, T. B. and Lighthill, M. J., "On cnoidal waves and bores," *Proc. R. Soc. London, Ser. A, Math. Phys. Sci.* **224**(1159), 448–460 (1954).
- Björnstad, M., Kalisch, H., Abid, M., Kharif, C., and Brun, M., "Wave breaking in undular bores with shear flows," *Water Waves* **3**, 473–490 (2021).
- Bonneton, P., van de Loock, J., Parisot, J.-P., Bonneton, N., Sottolichio, A., Detandt, G., Castelle, B., Mariu, V., and Pochon, N., "On the occurrence of tidal bores—the Garonne River case," *J. Coastal Res.* **64**, 1462–1466 (2011a).
- Bonneton, P., Parisot, J.-P., Bonneton, N., Sottolichio, A., Castelle, B., Mariu, V., Pochon, N., and van de Loock, J., "Large amplitude undular tidal bore propagation in the Garonne River, France," in *Proceedings of the 21st ISOPE Conference* (OnePetro, 2011b), pp. 870–874.
- Bonneton, P., Bonneton, N., Parisot, J.-P., and Castelle, B., "Tidal bore dynamics in funnel-shaped estuaries," *J. Geophys. Res. Oceans* **120**, 923–941, <https://doi.org/10.1002/2014JC010267> (2015).
- Bonneton, P., Filippini, A. G., Arpaia, L., Bonneton, N., and Ricchiuto, M., "Conditions for tidal bore formation in convergent alluvial estuaries," *Estuarine, Coastal Shelf Sci.* **172**, 121–127 (2016).
- Brühl, M., Prins, P. J., Ujvary, S., Barranco, I., Wahls, S., and Liu, P. L.-F., "Comparative analysis of bore propagation over long distances using conventional linear and KdV-based nonlinear Fourier transform," *Wave Motion* **111**, 102905 (2022).
- Castro-Ortiz, O. and Chanson, H., "Undular and broken surges in dam-break flows: A review of wave breaking strategies in a Boussinesq-type framework," *Environ. Fluid Mech.* **20**(6), 1383–1416 (2020).
- Castro-Ortiz, O. and Chanson, H., "Free surface profiles of near-critical instabilities in open channel flows: Undular hydraulic jumps," *Environ. Fluid Mech.* **22**(2–3), 275–300 (2022).
- Cea, L., Puertas, J., and Pena, L., "Velocity measurements on highly turbulent free surface flow using ADV," *Exp. Fluids* **42**(3), 333–348 (2007).
- Chanson, H., "Turbulence in positive surges and tidal bores. effects of bed roughness and adverse bed slopes," Department Technical Report No. CH68/08 (The University of Queensland, Brisbane, Australia, 2008).
- Chanson, H., "Current knowledge in hydraulic jumps and related phenomena. a survey of experimental results," *Eur. J. Mech. B* **28**, 191–210 (2009a).
- Chanson, H., "An experimental study of tidal bore propagation: The impact of bridge piers and channel construction," Hydraulic Model Report No. CH74/09 (The University of Queensland, Brisbane, Australia, 2009b).
- Chanson, H., "Undular tidal bores: Basic theory and free-surface characteristics," *J. Hydraul. Eng.* **136**, 940–944 (2010a).
- Chanson, H., "Unsteady turbulence in tidal bores: Effects of bed roughness," *J. Waterw., Port, Coastal, Ocean Eng.* **136**(5), 247–256 (2010b).
- Chanson, H., *Tidal Bores, Aegre, Mascaret, Pororoca: Theory and Observations* (World Scientific, Singapore, 2011a), p. 220.
- Chanson, H., "Undular tidal bores: Effect of channel constriction and bridge piers," *Environ. Fluid Mech.* **11**(4), 385–404 (2011b).
- Chanson, H., "Momentum considerations in hydraulic jumps and bores," *J. Irrig. Drain. Eng.* **138**(4), 382–385 (2012).
- Chanson, H., "Unsteady air entrainment in dam break waves and bores: Theoretical considerations," in *Proceedings of 23rd Australasian Fluid Mechanics Conference AFMC2022, Sydney, Australia, 4–8 December 2022* (Australasian Fluid Mechanics Society, 2022), Paper No. AFMC2022-011, p. 8.
- Chanson, H. and Tan, K. K., "Turbulent mixing of particles under tidal bores: An experimental analysis," *J. Hydraul. Res.* **48**(5), 641–649 (2010).
- Chanson, H., Reungoat, D., Simon, B., and Lubin, P., "High-frequency turbulence and suspended sediment concentration measurements in the Garonne River tidal bore," *Estuarine Coastal Shelf Sci.* **95**(2–3), 298–306 (2011).
- Chanson, H., Lubin, P., and Glockner, S., "Unsteady turbulence in a shock: Physical and numerical modelling in tidal bores and hydraulic jumps," in *Turbulence: Theory, Types and Simulation*, edited by Marcuso, R. J. (Nova Science Publishers, Hauppauge, 2012), Chap. 3, pp. 113–148.
- Chanson, H. and Lubin, P., "Mixing and sediment processes induced by tsunamis propagating upriver" in *Tsunamis: Economic Impact, Disaster Management and Future Challenges*, edited by Cai, T. (Nova Science Publishers, Hauppauge, 2013), Chap. 3, pp. 65–102.
- Chassagne, R., Filippini, A., Ricchiuto, M., and Bonneton, P., "Dispersive and dispersive-like bores in channels with sloping banks," *J. Fluid Mech.* **870**, pp. 595–616 (2019).
- Chugh, R. S., "Tides in Hooghly River," *Int. Assoc. Sci. Hydrol. Bull.* **6**(2), 10–26 (1961).
- Dhamankar, N. S., Blaisdell, G. A., and Lyrantzis, A. S., "Overview of turbulent inflow boundary conditions for large-eddy simulations," *AIAA J.* **56**(4), 1317–1334 (2018).
- Darcy, H. and Bazin, H., *Recherches Hydrauliques, 1ère et 2ème Parties* (Imprimerie Impériales, Dunod, Paris, 1865).
- Docherty, N. J. and Chanson, H., "Physical modeling of unsteady turbulence in breaking tidal bores," *J. Hydraul. Eng.* **138**, 412–419 (2012).
- Falgout, R., Jones, J., and Yang, U., "The design and implementation of HYPRE, a library of parallel high performance preconditioners," in *Numerical Solution of Partial Differential Equations on Parallel Computers*, Lecture Notes in Computational Science and Engineering, Vol. 51 (Springer, Berlin, Heidelberg, 2006), pp. 267–294.
- Fernando, R., Leng, X., and Chanson, H., "On unsteady velocity measurements and profiling in compression waves in an asymmetrical trapezoidal channel," *Exp. Therm. Fluid Sci.* **112**, 15 (2020).
- Filippini, A. G., Arpaia, L., Bonneton, P., and Ricchiuto, M., "Modeling analysis of tidal bore formation in convergent estuaries," *Eur. J. Mech. B* **73**, 55–68 (2019).
- Furgerot, L., "Hydrodynamic properties of tidal bore and its influence on sediment dynamics: Coupled approach in flume and *in situ* (see estuary, Mont Saint Michel Bay)," Ph.D. thesis (Université de Caen, France, 2014).
- Furgerot, L., Mouaze, D., Tessier, B., Perez, L., and Haquin, S., "Suspended sediment concentration in relation to the passage of a tidal bore (see river estuary, Mont Saint Michel Bay, NW France)," in 7th International Conference on Coastal Dynamics, Arcachon, France (2013).
- Furgerot, L., Mouazé, D., Tessier, B., Perez, L., Haquin, S., Weill, P., and Crave, A., "Sediment transport induced by tidal bores. An estimation from suspended matter measurements in the Sée River (Mont-Saint-Michel Bay, Northwestern France)," *C. R. Geosci.* **348**(6), 432–441 (2016).
- Furuyama, S. and Chanson, H., "A numerical study of open channel flow hydrodynamics and turbulence of the tidal bore and dam-break flows," Hydraulic Model Report No. CH66/08 (The University of Queensland, Brisbane, Australia, 2008).
- Goda, K., "A multistep technique with implicit difference schemes for calculating two- or three-dimensional cavity flows," *J. Comput. Phys.* **30**, 76–95 (1979).
- Hebenstreit, G., *Perspectives on Tsunami Hazard Reduction. Observations, Theory and Planning* (Kluwer Academic, Dordrecht, the Netherlands, 1997), p. 218.
- Henderson, F. M., *Open Channel Flow* (MacMillan Company, New York, 1966).
- Hornung, H. G., Willert, C., and Turner, S., "The flow field downstream of a hydraulic jump," *J. Fluid Mech.* **287**, 299–316 (1995).
- Jarrin, N., Benhamadouche, S., Laurence, D., and Prosser, R., "A synthetic-eddy method for generating inflow conditions for large-eddy simulations," *Int. J. Heat Fluid Flow* **27**(4), 585–593 (2006).

- Jarrin, N., "Synthetic inflow boundary conditions for the numerical simulation of turbulence," Ph.D. thesis (The University of Manchester, Manchester, United Kingdom, 2008).
- Jiang, H., Wang, L., Li, L., and Guo, Z., "Safety evaluation of an ancient masonry seawall structure with modified DDA method," *Comput. Geotech.* **55**, 277–289 (2014).
- Kalmbacher, K. D. and Hill, D. F., "Effects of tides and currents on tsunami propagation in large rivers: Columbia River, United States," *J. Waterw., Port, Coastal, Ocean Eng.* **141**(5), 04014046 (2015).
- Kang, S., Lightbody, A., Hill, C., and Sotiropoulos, F., "High-resolution numerical simulation of turbulence in natural waterways," *Adv. Water Resour.* **34**(1), 98–113 (2011).
- Kataoka, I., "Local instant formulation of two-phase flow," *Int. J. Multiphase Flow* **12**, 745–758 (1986).
- Keevil, C. E., Chanson, H., and Reungoat, D., "Fluid flow and sediment entrainment in the Garonne river bore and tidal bore collision," *Earth Surf. Processes Landforms* **40**(12), 1574–1586 (2015).
- Keylock, C. J., Hardy, R. J., Parsons, D. R., Ferguson, R. I., Lane, S. N., and Richards, K. S., "The theoretical foundations and potential for large-eddy simulation (LES) in fluvial geomorphic and sedimentological research," *Earth-Sci. Rev.* **71**(3–4), 271–304 (2005).
- Kiri, U., Leng, X., and Chanson, H., "Transient secondary currents behind a compression wave in an irregular channel," *Environ. Fluid Mech.* **20**(4), 1053–1073 (2020a).
- Kiri, U., Leng, X., and Chanson, H., "Positive surge propagating in an asymmetrical canal," *J. Hydro-Environment Res.* **31**, 41–47 (2020b).
- Khezri, N., "Modelling turbulent mixing and sediment process beneath tidal bores: Physical and numerical investigations," Ph.D. thesis (The University of Queensland, Brisbane, Australia, 2014).
- Khezri, N. and Chanson, H., "Undular and breaking bores on fixed and movable gravel beds," *J. Hydraul. Res.* **50**, 353–363 (2012).
- Kjerfve, B. and Ferreira, H. O., "Tidal bores: First ever measurements," *Cincia Cultura* **45**, 135–138 (1993).
- Kobayashi, D. and Uchida, T., "Experimental and numerical investigation of breaking bores in straight and meandering channels with different Froude numbers," *Coastal Eng. J.* **64**(3), 442–457 (2022).
- Koch, C. and Chanson, H., "Turbulent mixing beneath an undular bore front," *J. Coastal Res.* **244**(4), 999–1007 (2008).
- Koch, C. and Chanson, H., "Turbulence measurements in positive surges and bores," *J. Hydraul. Res.* **47**(1), 29–40 (2009).
- Krautwald, C., von Häfen, H., Niebuhr, P., Vögele, K., Schürenkamp, D., Sieder, M., and Goseberg, N., "Large-scale physical modeling of broken solitary waves impacting elevated coastal structures," *Coastal Eng. J.* **64**, 169–189 (2022).
- Laut, L. L. M., Ferreira, D. E. D. S., Santos, V. F., Figueiredo, Jr., A. G., Carvalho, M. D. A., and Machado, O. F., "Foraminifera, thecamoebians and palynomorphs as hydrodynamic indicators in Araguari Estuary, Amazonian Coast, Amapa State–Brazil," *Anu. Inst. Geocienc.* **33**(2), 52–65 (2010).
- Lemoine, R., "Sur les ondes positives de translation dans les canaux et sur le ressaut ondulé de faible amplitude," *Houille Blanche* **2**, 183–185 (1948).
- Leng, X., "A study of turbulence: The unsteady propagation of bores and surges," Ph.D. thesis (The University of Queensland, Brisbane, Australia, 2018).
- Leng, X. and Chanson, H., "Air–water interaction and characteristics in breaking bores," *Int. J. Multiphase Flow* **120**, 103101 (2019).
- Leng, X., Simon, B., Khezri, N., Lubin, P., and Chanson, H., "CFD modelling of tidal bores: Development and validation challenges," *Coastal Eng. J.* **60**(4), 423–436 (2018).
- Liggett, J. A., *Fluid Mechanics* (McGraw-Hill, New York, 1994).
- Lin, C., Kao, M. J., Yuan, J. M., Raikar, R. V., Wong, W.-Y., Yang, J., and Yang, R. Y., "Features of the flow velocity and pressure gradient of an undular bore on a horizontal bed," *Phys. Fluids* **32**(4), 043603 (2020a).
- Lin, C., Kao, M. J., Yuan, J. M., Raikar, R. V., Hsieh, S. C., Chuang, P. Y., Syu, J. M., and Pan, W. C., "Similarities in the free-surface elevations and horizontal velocities of undular bores propagating over a horizontal bed," *Phys. Fluids* **32**(6), 063605 (2020b).
- Liu, H., Shimazono, T., Takagawa, T., Okayasu, A., Fritz, H. M., sato, s., and tajIMA, T., "The 11 March 2011 Tohoku tsunami survey in Rikuzentakata and comparison with historical events," *Pure Appl. Geophys.* **170**, 1033–1046 (2013).
- Lubin, P., "Large eddy simulation of plunging breaking waves," Ph.D. thesis (Université Sciences et Technologies - Bordeaux I, 2004).
- Lubin, P. and Glockner, S., "Numerical simulations of three-dimensional plunging breaking waves: Generation and evolution of aerated vortex filaments," *J. Fluid Mech.* **767**, 364–393 (2015).
- Lubin, P., Glockner, S., and Chanson, H., "Numerical simulation of a weak breaking tidal bore," *Mech. Res. Commun.* **37**(1), 119–121 (2010a).
- Lubin, P., Chanson, H., and Glockner, S., "Large eddy simulation of turbulence generated by a weak breaking tidal bore," *Environ. Fluid Mech.* **10**(5), 587–602 (2010b).
- Madsen, P. A., Simonsen, H., and Pan, C. H., "Numerical simulation of tidal bores and hydraulic jumps," *Coastal Eng.* **52**(5), 409–433 (2005).
- Madsen, P. A., Fuhrman, D. R., and Schäffer, H. A., "On the solitary wave paradigm for tsunamis," *J. Geophys. Res.* **113**, C12012, <https://doi.org/10.1029/2008JC004932> (2008).
- Malandain, J. J., "La Seine au temps du Mascaret ('The Seine River at the Time of the Mascaret')," *Le Chasse-Marée* **34**, 30–45 (1988) (in French).
- Marche, C., Beauchemin, P., and Kayloubi, A. E., "Etude numérique et expérimentale des ondes secondaires de Favre consécutives à la rupture d'un barrage," *Can. J. Civ. Eng.* **22**(4), 793–801 (1995).
- Marquillie, M. and Ehrenstein, U., "On the onset of nonlinear oscillations in a separating boundary-layer flow," *J. Fluid Mech.* **490**, 169–188 (2003).
- Montes, J. S., *Hydraulics of Open Channel Flow* (ASCE Press, 1998), p. 697.
- Montes, J. S. and Chanson, H., "Characteristics of undular hydraulic jumps: Experiments and analysis," *J. Hydraul. Eng.* **124**, 192–205 (1998).
- Moore, W. U., *Further Report on the Bore of T sien-Tang-Kiang* (Hydrographic Office, Admiralty, London, 1893).
- Mouaze, D., Chanson, H., and Simon, B., "Field measurements in the tidal bore of the Sélune River in the Bay of Mont Saint Michel (September 2010)," Hydraulic Model Report No. CH81/10 (The University of Queensland, Brisbane, Australia, 2010).
- Nachbin, A. and Simoes, V. S., "Solitary waves in open channels with abrupt turns and branching points," *J. Nonlinear Math. Phys.* **19**(1), 116 (2012).
- Navarre, P., "Aspects physiques du caractère ondulatoire du mascaret en Dordogne," D.E.A. thesis (Université de Bordeaux, France, 1995).
- Nezu, I. and Nakagawa, H., *Turbulence in Open-Channel Flows* (Balkema, Rotterdam, Brookfield, 1993).
- Pan, D. Z. and Chanson, H., "Physical modelling of tidal bore dyke overtopping: Implication on individuals' safety," in *Proceedings of the 36th IAHR World Congress, the Hague, The Netherlands, 27 June–3 July, 2015* (IAHR, 2015), pp. 3824–3831.
- Patankar, S. V., *Numerical Heat Transfer and Fluid Flow* (Hemisphere Publishing Corporation McGraw-Hill, Washington, New York, 1980).
- Peregrine, D. H., "Calculations of the development of an undular bore," *J. Fluid Mech.* **25**(2), 321–330 (1966).
- Putra, Y. S., Beaudoin, A., Rousseaux, G., Thomas, L., and Huberson, S., "2D numerical contributions for the study of non-cohesive sediment transport beneath tidal bores," *C. R. Méc.* **347**(2), 166–180 (2019).
- Rayleigh, L., "Note on tidal bores," *Proc. R. Soc. A: Math., Phys. Eng. Sci.* **81**, 448–449 (1908).
- Reungoat, D., Chanson, H., and Caplain, B., "Sediment processes and flow reversal in the undular tidal bore of the Garonne River (France)," *Environ. Fluid Mech.* **14**(3), 591–616 (2014).
- Reungoat, D., Leng, X., and Chanson, H., "Successive impact of tidal bores on sedimentary processes: Arcins channel, Garonne River," *Estuarine Coastal Shelf Sci.* **188**, 163–173 (2017).
- Rouse, H., *Fluid Mechanics for Hydraulic Engineers* (McGraw-Hill Publication, New York, 1938).
- Roy-Biswas, T., Dey, S., and Sen, D., "Modeling positive surge propagation in open channels using the Serre-Green-Naghdi equations," *Appl. Math. Modell.* **97**, 803–820 (2021).
- Roy-Biswas, T. and Sen, D., "Critical analysis of turbulence models for simulating positive surge waves in open channels in a RANS-VOF setup," *Environ. Fluid Mech.* **22**, 1253–1281 (2022).
- Rulifson, R. A. and Tull, K. A., "Striped bass spawning in a tidal bore river: The Shubenacadie Estuary, Atlantic Canada," *Trans. Am. Fish. Soc.* **128**(4), 613–624 (1999).

- Ryabenko, A., "Representation of a wave jump and group of translation waves as a combination of a solitary wave and cnoidal waves," *Hydrotech. Constr.* **32**(5), 246–252 (1998).
- Sagaut, P., *Large Eddy Simulation for Incompressible Flows: An Introduction*, 3rd ed. (Springer-Verlag Berlin and Heidelberg, Berlin, Heidelberg, New York, 2006).
- Sandover, J. A. and Taylor, C., "Cnoidal waves and bores," *Houille Blanche* **48**(3), 443–445 (1962).
- Sandover, J. A. and Zienkiewicz, O. C., "Experiments on surge waves," *Water Power* **9**, 418–424 (1957).
- Shi, R., "Modelling air-water turbulence and properties in unsteady breaking bore," Ph.D. thesis (The University of Queensland, 2022).
- Shi, R., Wüthrich, D., and Chanson, H., "Air-water properties of unsteady breaking bores. Part 1: Novel Eulerian and Lagrangian velocity measurements using intrusive and non-intrusive techniques," *Int. J. Multiphase Flow* **159**, 104338 (2023a).
- Shi, R., Wüthrich, D., and Chanson, H., "Air-water properties of unsteady breaking bore. Part 2: Void fraction and bubble statistics," *Int. J. Multiphase Flow* **159**, 104337 (2023b).
- Smagorinsky, J., "General circulation experiments with the primitive equations," *Mon. Wea. Rev.* **91**, 99–164 (1963).
- Simon, B., "Effects of Tidal bores on turbulent mixing: A numerical and physical study in positive surges," Ph.D. thesis (The University of Queensland, Brisbane, Australia, 2014).
- Simon, B. and Chanson, H., "Turbulence measurements in tidal bore-like positive surges over a rough bed," Hydraulic Model Report No. CH90/12 (The University of Queensland, Brisbane, Australia, 2013).
- Simpson, J. H., Fisher, N. R., and WILES, P., "Reynolds stress and TKE production in an estuary with a tidal bore," *Estuarine, Coastal Shelf Sci.* **60**(4), 619–627 (2004).
- Soares Frazao, S. and Zech, Y., "Undular bores and secondary waves-experiments and hybrid finite-volume modelling," *J. Hydraul. Res.* **40**, 33–43 (2002).
- Stoker, J. J., *Water Waves: The Mathematical Theory with Applications* (Interscience Publisher, Inc., New York, 1957).
- Thomas, L. and David, L., "Eulerian and Lagrangian coherent structures in a positive surge," *Exp. Fluids* **63**(2), 43 (2022).
- Tolkova, E., "Observations of tsunamis in rivers," in *Tsunami Propagation in Tidal Rivers*, Springer Briefs in Earth Sciences (Springer, Cham, 2018).
- Tolkova, E., Tanaka, H., and Roh, M., "Tsunami observations in rivers from a perspective of tsunami interaction with tide and riverine flow," *Pure Appl. Geophys.* **172**, 953–968 (2015).
- Treske, A., "Undular bores (Favre-waves) in open channels—experimental studies," *J. Hydraul. Res.* **32**, 355–370 (1994).
- Violeau, D., "Contribution to the theory of undular bores. A journey around the Korteweg-de Vries equation," IAHR Monograph No. 96, 2022.
- Winckler, P. and Liu, P., "Long waves in a straight channel with non-uniform cross-section," *J. Fluid Mech.* **770**, 156–188 (2015).
- Wolanski, E., Williams, D., Spagnola, S., and Chanson, H., "Undular tidal bore dynamics in the Daly Estuary, Northern Australia," *Estuarine, Coastal Shelf Sci.* **60**(4), 629–636 (2004).
- Wüthrich, D., Shi, R., and Chanson, H., "Strong free-surface turbulence in breaking bores: A physical study on the free-surface dynamics and air-water interfacial features," *J. Fluid Mech.* **924**, 37 (2021).
- Yeh, H., Liu, P., and Synolakis, C., *Long-Wave Runup Models* (World Scientific, Singapore, 1996), p. 403.
- Yeh, H., Tolkova, E., Jay, D., Talke, S., and Fritz, H., "Tsunami hydrodynamics in the Columbia River," *J. Disaster Res.* **7**(5), 604–608 (2012).
- Youngs, D. L., "Time-dependent multi material flow with large fluid distortion," in *Numerical Methods for Fluid Dynamics*, Conference Series (Institute of Mathematics and Its Applications), edited by Morton, K. W. and Baines, M. J. (Academic Press, London, New York, 1982).
- Zienkiewicz, O. C. and Sandover, J. A., "The undular surge wave," in *Proceedings of the 7th IAHR Congress, Lisbon, Portugal* (IAHR, 1957), Vol. II, Paper No. D25, pp. D1–D11.